Molecular dynamics simulations of water and acetonitrile mixtures in external electric field

Dissertation for obtaining the degree of "Doctor of Natural Sciences" in the Department of Physics, Mathematics and Computer Science at the Johannes Gutenberg University in Mainz

Anastasios Sourpis born in Amarousion Attikis, Greece

Mainz, 11 June 2024

to my parents and my siblings

Declaration

I, Anastasios Sourpis, hereby certify that I have completed this work independently and not used any sources or aids (including electronic media and online sources) other than those indicated. I am aware that it constitutes an attempt at cheating or a breach of regulation if this statement proves to be untrue. section 17, para. 3 and 5 shall apply in such case.

11 June 2024

Acknowledgements

First of all, I would like to thank my supervisor *Friederike Schmid*, initially for allowing me to work on an exciting topic and for the opportunity to evolve scientifically during my Ph.D.. *Nancy C. Forero-Martinez* for her support when things were not working well and being patient. *Daniela Reibel-El Batanony* for her awareness of resolving all the bureaucracy issues and being always there when something came up and for her support even in new unknown situations during COVID-19 she did everything work smoothly. *Mariana Cosarinsky* and GRK's co-student speaker *Oliver* for their help in co-organizing a very successful workshop and running smoothly the GRK 2516 initiative. *Pol Besenius* for his awareness and approachability always being available for discussions and simultaneously steering the wheel of GRK 2516.

Nothing could be done without you guys. I will start with seniority (experience). First my friend *Le* (oder Lè in French). Thank you for your way of *to do things*, and for the amazing dinners! Then my office-mates *Marios*, *Niklas*, and *Kai*. Thank you *Marios* for Lubenizing the office spirit, and going against *Niklas* spirit of harmonizing life with tea and educational physics :) thank you *Niklas*. Also, *Yannick*, *Jan*, *Simon*, and *Maurice* (Mavrikio) for the discussions during lunch break. The basketball players *Emanuelle* (Dr. Zippo), *Kai*, and *Yashraj* (*Yash*) for the nice times on the court or the grass in case of Spikeball. *Ranajay* (*Rana*), and *Gaurav* for their unique way of making things more enjoyable and funny, I will not forget the amazing Indian and Greek dinners.

Elleonora, thank you for your support, your friendship was uncountable, I will never forget our Sunday lunches and evening coffees at the Rhine. *Christos & Adriana* thank you for the unforgettable dinners and especially *Christos* for the amazing greek guitar night!

Of course *Kostas* and *Yiorgos* (*Chiotis* (the guy from Chios, Greek Island)) the "*Greek mafia*" of German classes. Next, *Eleni* without her classes I would have not met these amazing guys, and also for her unique way of simplifying the complexity of the German language.

During my Ph.D. journey, I would like to thank my best friends *Thanos*, *George* and *Yiannis* for their friendship through the years. I will never forget 12 October 2020, as one of my best moments here in Mainz because of you guys!

Last but not least, I want to acknowledge my beloved parents *Yiannis* and *Effie* for their endless love and support through the years. Finally, my siblings *Giorgos* and *Alexandra* for their support and encouragement and being always next to me.

Abstract

Electrochemistry is a discipline promising to advance material science towards more environmentally friendly and sustainable technologies for energy solutions. Electrochemical systems are usually composed of interacting complex molecules, making understanding collective effects limited for macroscopic experiments. Computer simulations offer a way to obtain insights in-silico. In particular, molecular dynamics simulations, with detailed interatomic potentials, allow us to rationalize experimental results by exploring the dynamics of physical systems through virtual experiments.

In the first part of this thesis, I systematically review molecular dynamics simulation methods providing the foundation for preparing our physical system in-silico. I introduce the basic principles of an all-atom molecular simulation within the framework of statistical physics and discuss in detail the treatment of electrostatic interactions and the importance of dielectric boundary conditions. In the second part of this thesis, I present our molecular dynamics study of a liquid system composed of water and acetonitrile molecules and its response to an external electric field. This mixture exhibits unique properties, including a distinctive electrical conductivity detection in the absence of an electrolyte in novel electrolysis flow cells. However, the underlying physical mechanism behind this phenomenon remains unknown. As a first step to understanding this mechanism, this work focuses on the bulk system structure and how a macroscopic external electric field influences its properties.

Zusammenfassung

Die Elektrochemie birgt grosses Potential, in den Materialwissenschaften die Entwicklung umweltfreundlicherer und nachhaltigerer Technologien für Energielösungen voranzutreiben. Elektrochemische Systeme bestehen in der Regel aus komplexen, miteinander wechselwirkenden Molekülen, was die Analyse kollektiver Effekte in makroskopischen Experimenten erschwert. Computersimulationen bieten einen Weg, Erkenntnisse in Silico zu gewinnen. Insbesondere atomistisch detaillierte molekulardynamische Simulationen ermöglichen es, experimentelle Ergebnisse einzuordnen, indem die Dynamik physikalischer Systeme durch virtuelle Experimente erkundet wird.

Im ersten Teil dieser Arbeit wird eine Übersicht über verschiedene Methoden der Molekulardynamiksimulationen gegeben, die dieser Arbeit zugrundeliegen. Ich führe die grundlegenden Prinzipien atomistischer Simulationen auf Basis der statistischen Physik ein und diskutiere ausführlich die Behandlung elektrostatischer Wechselwirkungen und die Bedeutung von dielektrischen Randbedingungen. Im zweiten Teil der Arbeit präsentiere ich eine molekulardynamische Studie von Wasser/Azetonitril-Mischungen, und ihrer Reaktion auf externe elektrisches Felder. Diese Mischungen weisen einzigartige Eigenschaften auf. Beispielsweise wurden in neuartigen Elektrolyse-Flusszellen beobachtet, dass sie in Abwesenheit eines Leitsalzes leitfähig sein können. Der physikalische Mechanismus, der diesem Phänomen zugrunde liegt, ist jedoch unbekannt. Als ersten Schritt zu seinem Verständnis untersucht die vorliegende Arbeit die Struktur der Flüssigkeit im Volumen und die Veränderungen, die durch ein makroskopisches externes elektrisches Feld induziert werden.

Contents

List of Figures

List of Tables

Chapter 1

Introduction

Electrochemistry: Electrochemistry, from a physical perspective, relates phenomena between two conductors: the electron conductor, the electrode, and the ion conductor, the electrolyte [1]. The electric double layer (EDL), a unique interface formed between the electrode and electrolyte, is characterized by distinct physical [2] and chemical properties [3], in addition to hosting various electrochemical reactions. Two primary reactions occur between electrodes and solution and play an essential role in hydrogen energy production systems: the hydrogen evolution reaction (HER) and the hydrogen oxidation reaction (HOR). The pH modulation influences the EDL dynamics, affecting the HER and HOR activities [4]. The hydrogen bond network is the medium through which the pH impacts the EDL [5]. Recent investigations show different responses of the EDL's structural configuration to anodic and cathodic charging [6]. In particular, it has been demonstrated that the electric field influences the interfacial reorganization of water, subsequently affecting the HER/HOR activity, particularly in alkaline environments [7]. This result emphasizes the tunability of the EDL, presenting opportunities for manipulation through pH adjustments or by controlling the electric field at the electrode/electrolyte interface. In this context, this thesis explores the multifaceted nature of electrochemical processes, focusing on the interdependence between the hydrogen bond networks' structural phase transitions induced by electric fields.

Acetonitrile/Water: Acetonitrile (CCN)/water mixtures have gathered considerable attention within the electrochemical community [8, 9]. Characterized by distinct electric and magnetic properties, acetonitrile possesses a dielectric constant approximately half that of water $\varepsilon_{CCN} \approx \varepsilon_{H_2O}/2$. This characteristic is closely tied to its response to the electric field, prompting a comprehensive examination of the inherent structural properties of CCN mixtures to reveal pertinent electrical phenomena. The CCN/water mixtures operate within the framework of microheterogeneities governed by the hydrogen bond network. Here, CCN serves as a confinement matrix for water [10]. This matrix effect, resulting from

intricate molecular interactions, sets the stage for identifying fundamental properties within these mixtures. This thesis work has elucidated two significant properties of CCN/water mixtures, strongly correlated with fundamental characteristics influencing the HER and the HOR. Recent reports have indicated a noteworthy increase in the HER activity in the presence of CCN [9]. The dielectric contrast between acetonitrile and water, coupled with the microheterogeneities shaped by the hydrogen bond network, emphasizes the potential impact of these mixtures on electrochemical activities. The interplay between CCN's role as a confinement matrix and its influence on the HER activity opens avenues for understanding and manipulating electrochemical processes.

Physical Electrochemistry: In electrochemistry, the influence of the hydrogen bond network and the electric field near the interface plays a central role in governing the primary electrochemical reactions, HER and HOR. This influence persists even under weakened EDLs, which is characteristic of low ionic concentration scenarios. This thesis aims to investigate the properties of electrified solutions, specifically to elucidate the topology of the hydrogen bond network and to understand the system's response to an external electric field. This research aims to provide an approach to understanding complex electrochemical phenomena using classical molecular dynamics, focusing on the electrical conductivity in narrow-gap electrolysis flow cells [11]. This thesis adopts a molecular dynamics approach as a powerful tool for exploring the dynamics between the hydrogen bond network and the electric field in electrified solutions. Classical molecular dynamics simulations allow for a detailed and comprehensive investigation of these systems, offering insights into electrochemical processes without explicit consideration of electronic degrees of freedom. The primary aim is to describe how the topology of the hydrogen bond network influences electrochemical activities and how the electric field's response contributes to the overall behavior of electrified solutions.

Publication

Chapter 4 reproduces the publication "The effect of electric fields on the structure of water/acetonitrile mixtures", A. I. Sourpis, N. C. Forero-Martinez, F. Schmid, J. Electrochem. Soc. 170, 083508 (2023). The research was carried out by myself. The text of the publication was drafted by myself and then finalized jointly by all authors.

Part I

Chapter 2

Molecular Dynamics Simulations

2.1 Statistical mechanics

2.1.1 Molecular simulation from algorithms to applications

Molecular dynamics simulations are a stepping-stone computational technique to study physical systems. Especially for molecular systems at the nanoscale, where the system's equations of motion are integrated based on classical *force fields* (see section 2.2). The computational complexity increases as a function of the number of particles N. The number of particles is related to the system size. A many-body classical system is a physical system governed by thermodynamic laws. This many-body system can describe thermodynamic equilibrium or out-of-equilibrium systems. Here, we mainly focus on systems in thermodynamic equilibrium.

Microscopically, the system is governed by the force fields and the electrostatic interactions and it evolves based on the laws of classical mechanics. Macroscopically, the system is governed by the laws of thermodynamics. A macrostate is a unique state of the system described by a unique set of macroscopic (averaged values), i.e. (N, V, T) where N is the total number of particles, V is the system's volume and T is the system's temperature. One macrostate corresponds to a set of microstates called ensemble $\mathscr{F}$. Every macrostate has its specific ensemble, i.e. $\mathscr{F} = \mathscr{F}(N,V,T)$, $\mathscr{G} = \mathscr{G}(N,p,T)$ etc. The $\mathscr{F} = \mathscr{F}(N,V,T)$ is called *canonical ensemble* and corresponds to a physical system in thermal equilibrium with a large heat bath. Since this is a macrostate, it needs to fulfil the law of thermodynamics. The first law of thermodynamics is written as

$$dU = \delta Q + dW, \tag{2.1}$$

where U is the system's internal energy; this can be changed via thermal Q or work W exchange.

Next, using the second law of thermodynamics, the entropy S is given by

$$dS = \frac{\delta Q}{T}. \tag{2.2}$$

The macrostate $F = F(N,V,T)$ then fulfil the macroscopic equation

$$dF = d\left(U - TS\right) = -SdT + pdV + \mu dN \tag{2.3}$$

where $F(N,V,T) = U - TS$ is the free energy and is useful for deriving many macroscopic quantities. Statistical mechanics connects the macroscopic states of the system to its microstates. The canonical ensemble is a Boltzmann distribution where the probability of a microscopic state i is defined as

$$p_i = \frac{e^{-\beta H^{(i)}\left(\{\mathbf{r}^N_{(i)},\mathbf{p}^N_{(i)}\}\right)}}{Z(N,V,T)}, \tag{2.4}$$

where $\beta = 1/k_B T$, $H^{(i)} = K^{(i)} + U^{(i)}_{int.}$ is the microscopic energy , K^i and $U^{(i)}_{int.}$ are the microscopic kinetic and potential energy of the microstate i and $Z(N,V,T) = \int d\mathbf{r}^{(N)} d\mathbf{p}^{(N)} e^{-H^{(i)}\left(\{\mathbf{r}^N_{(i)},\mathbf{p}^N_{(i)}\}\right)}$ is the canonical partition function. Eq. 2.4 is crucial in statistical mechanics since it can be used to define the average value of an observable quantity.

Molecular simulations: Molecular dynamics simulation is useful for measuring properties corresponding to experimentally observed quantities. The experimental quantities are average properties over the time of measurement. Hence, molecular dynamics simulations are helpful in for comparing the average physical values obtained from a sample of positions or snapshots called *trajectories* $\{t,\mathbf{r},\mathbf{v}\}$ against experimental observable quantities as counterparts. In practice a microstate is a snapshot of the system of particles in a specific macrostate (N,V,T). A snapshot is an instant collective configuration of systems' particles. Such a collection of snapshots (trajectory) is another representation of the ensemble $\mathscr{F}$. This is the key point of how molecular dynamics simulations work. First, we should understand what phenomena can occur in a classical system in equilibrium. For instance, if we would like to equilibrate a system of particles in a thermal bath, the embedded system should "communicate/interact" via the bath until it reaches the temperature T_{equil}. This is achieved by rescaling the velocities each step dt [12]. Now, the microstates are governed by Newton's equations of motion. Solving the equations of motion for every particle of the system

$$\mathbf{F} = m\dot{\mathbf{v}} \rightarrow \{t,\mathbf{r},\mathbf{v}\}, \tag{2.5}$$

we can derive the proper ensemble of trajectories $\{t, \mathbf{r}, \mathbf{v}\}$.

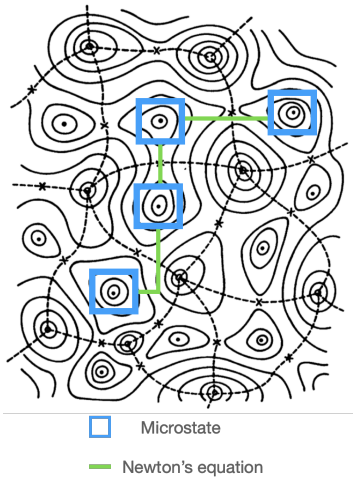

Figure 2.1 Potential energy surface in the phase space, as illustrated by [13]. How the molecular dynamics simulations work, collecting an ensemble of microstates (coordinates $\{\mathbf{x}_i, \mathbf{v}_i\}$) blue boxes which have been derived by Newton's equation green lines.

Equations of motion: In phase space, starting from tow different initial points (initial conditions) close to each other and let the system to evolve accordingly in time, then the corresponding two trajectoral points will diverge exponentially. This is called Lyapunov instability [14]. In the case of molecular dynamics simulations, we want to predict the average behavior of the system, so we do not worry so much about the Lyapunov instability.

Proper algorithm: The numerical scheme for solving Newtons' equations must be *symplectic* (in true Hamiltonian dynamics the volume element in phase space is preserved) and *time reversible* [14]. These two requirements should be fulfilled by the trajectories of the ensemble $\mathscr{F}(\{t, \mathbf{r}^{(N)}, \mathbf{v}^{(N)}\}_{trj})$ to have physical meaning [14, 15]. The integration scheme also defines the ergodicity of the collection $\mathscr{F}$ [12].

Ergodicity: Ergodicity is crucial in molecular dynamics simulations. In Fig. 2.1 we give a schematic explanation of ergodicity. Let's consider a system of N particles on a specific macrostate i.e. (N, V, E), and replicate this system n-times. Each replica is the system with different initial conditions (black dashed box) averaged over these correspond to ensemble average $\langle ... \rangle$. However, we can also pick an initial condition and let the system evolve following the equations of motion and then average $\overline{(...)}$. The ergodic principle can be postulated as

$$\overline{\rho_i(r)} = \langle \rho_i(r) \rangle_{NVE} \,. \tag{2.6}$$

In this present work, the thermostat of canonical sampling through velocity rescaling [12] has been used as a numerical scheme for microcanonical (N,V,E) and canonical (N,V,T) ensemble simulations. During the (N,p,T) simulations the Parrinello-Rahman thermostat [16] was used.

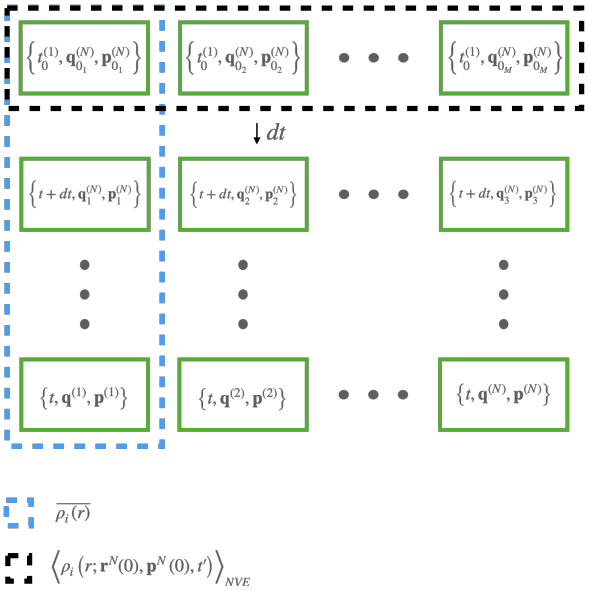

Figure 2.2 Phase space ensembles and molecular dynamics simulations.

2.1.2 Linear response

The statistical ensemble $\mathscr{F}(q,p)$ (i.e. (N,V,T)) is the collection of the microstates in phase space. The evolution of $\mathscr{F}(q,p)$ in phase space is written as

$$\frac{\partial \mathscr{F}}{\partial t} = (\mathscr{H}, \mathscr{F}), \tag{2.7}$$

where $(\mathscr{H}, \mathscr{F})$ is the Poisson's bracket

$$(\mathscr{H}, \mathscr{F}) = \sum \left(\frac{\partial \mathscr{H}}{\partial q} \frac{\partial \mathscr{F}}{\partial p} - \frac{\partial \mathscr{H}}{\partial p} \frac{\partial \mathscr{F}}{\partial q} \right), \tag{2.8}$$

with $\mathscr{H}$ the system's Hamiltonian.

In equilibrium, these microstates correspond to systems' potential energy minima so eq. 2.8 gives us $(\mathscr{H}, \mathscr{F}) = 0$ (see Fig. 2.1). In the case where an external electric field is applied, the phase space should be different. The evolution of the phase space density during the perturbation is expressed by [17]

$$\frac{\partial \mathscr{F}'(t)}{\partial t} = \underbrace{\left(\mathscr{H}, \mathscr{F}'\right)}_{\textit{perturbative density}} + \underbrace{\left(\mathscr{H}'(t), \mathscr{F}\right)}_{\textit{perturbative Hamiltonian}} . \tag{2.9}$$

Where $\mathscr{F}'$ corresponds to a phase space density evolving with a perturbed collected Hamiltonian $\mathscr{H}'$. If this new $\mathscr{F}'$ is linear $\mathscr{F}' = \mathscr{F} + \delta f$, then we can apply linear response relations to calculate physical quantities. Furthermore, the linear response regime can be observed by studying a different $\mathscr{H}'$. In our case, we study the response to an the electric field effect. $\mathscr{H}' = \mathscr{H}_0 - \mathbf{EM}$, with $\mathscr{H}_0$ the system's Hamiltonian without external electric field and $\mathbf{E}$ the external electric field, which is coupled with the system's total polarization $\mathbf{M}$. The Hamiltonian $\mathscr{H}$ is referred to a system embeded into a conductor (see Chapter 3.4). Hence, the system can be manipulated by varying the external electric field $\mathbf{E}$ and computing its response in this case, the polarization as a function of the strength of the electric field. In the linear response regime, a given system response to an external perturbation is expressed in terms of the fluctuation properties of the system in thermal equilibrium as the linear response theory provides the general proof of the fluctuation-dissipation theorem [18].

2.2 Force fields

2.2.1 Force field (Acetonitrile)

The potential energy is crucial since it contains the dynamical description of our system. Here, we need to clarify that the potential energy in molecular dynamics simulations approximates of the real systems' interactions. We implement classical molecular dynamics simulations, where the energy scale of our systems is in k_BT and the time scale is in ns with time steps of sampling on fs. Electronic degrees of freedom are not considered explicitly.

2.2.2 Atoms

Everything starts from the beginning. Atoms are the fundamental components of matter. Atoms are characterized by their mass m and atomic number Z some can also be charged (ions). Atoms also interact with each other via Lennard-Jones interactions. The most common Lennard-Jones potential is given by

$$U_{LJ}(r) = 4\varepsilon \left[\left(\frac{\sigma}{r}\right)^{12} - \left(\frac{\sigma}{r}\right)^{6} \right], \tag{2.10}$$

where σ and ε defines how deep and broad is the LJ potential accordingly.

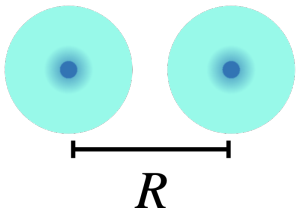

Figure 2.3 Lennard-Jones potential. R is the distance between the atomic centers.

The Lennard-Jones model is the collective interaction of the electrons between the atoms. In his seminal work, Lenard-Jones [19] defined van der Waals fields by a simple molecular model, where the dynamics of the electron is described as a linear vibration around the nucleus.

Then, we consider that the oscillator is subject to the field of a rigid dipole μ. The potential of the electron is $-2\mu ez/R^3$ (with z a dimensional quantity) and the polarization energy is written as the square of the field

$$Pol : -2e^2\mu^2/kR^6, \tag{2.11}$$

where k is the oscillator's strength constant.

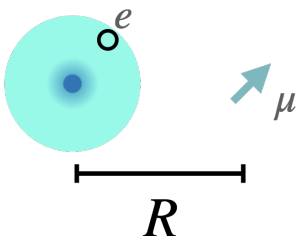

Figure 2.4 Lennard-Jones potential attractive term

The repulsive potential term is due to Pauli's exclusion principle. The attractive term is also due to a quantum mechanical effect based on a second-order perturbation theory. The attractive term is due to dynamic polarization; the motion of a system of two quantum oscillators in phase [19].

Last, a system of interacting particles should be sufficient to know the four physical quantities $\{m, Z, q, \varepsilon, \sigma\}$. In the case of mixtures of atoms, the Lennard-Jones potential eq. 2.10 can be approached for a collection of different atoms by implementing the Lorentz-Berthelot combination rules,

$$\sigma_{ij} = \frac{1}{2}\left(\sigma_{ii}+\sigma_{jj}\right) \tag{2.12}$$

$$\varepsilon_{ij} = \left(\varepsilon_{ii}\varepsilon_{jj}\right)^{1/2} \tag{2.13}$$

`GROMACS` and `atomtype.itp`

Atoms' information exists in every MD simulation package. In the case of the simulation package `GROMACS` [20], this is included in the file `atomtypes.itp`. All the physical quantities mentioned above $\{m, Z, q, \varepsilon, \sigma\}$ are defined and associated with a unique atom.

Table 2.1 Atomic definition of the CCN molecule

[atoms]						
name	*atomic number*	*mass*	*charge*	*ptype*	σ	ε
N1	7	14.01	0.0000	A	3.33700e-01	6.99860e-01
C1	6	12.01	0.0000	A	3.75290e-01	4.84670e-01
C2	6	12.01	0.0000	A	3.39960e-01	4.57720e-01
H21	1	1.008	0.0000	A	2.45510e-01	1.00000e-05
H22	1	1.008	0.0000	A	2.45510e-01	1.00000e-05
H23	1	1.008	0.0000	A	2.45510e-01	1.00000e-05

In `GROMACS` an extra column *ptype* exists, where the particle type is included. Three particles types are available, atom *A*, shell `S` and virtual site *V* or *D*.

2.3 Molecules

2.3.1 Bonds

Atoms can bind with each other forming molecules. These are called bonded interactions. This section's roadmap starts with describing chemical bonds with their energy scales. The quantum dynamical description of chemical bonds follows and finally, the classical interpretation is given in terms of classical dynamics and Euclidean geometry.

2.3.2 Energy scale

Covalent bonds are a special type of bonds, such as two hydrogen atoms make a molecule H_2. *Energy* is released when the electrons associated with the two hydrogen atoms form a covalent bond $-435\ kJ/mol$ [21]. Another characteristic of the H_2 is the distance between

the two atoms or *bond length*. *Energy* and *bond length* play a significant role and specify some unique molecular properties. For comparison, hydrogen bonds and van der Waals interactions between molecules are weaker than a few tens of kJ/mol [22].

2.3.3 Classical representation

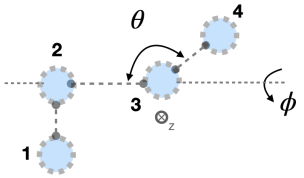

Figure 2.5 Bonds, a general case

The bond stretching energy between two covalently bonded atoms i and j is described by an harmonic potential:

$$V_{bond}(r_{ij}) = \frac{1}{2}k^b_{ij}\left(r_{ij} - b_{ij}\right)^2, \tag{2.14}$$

where k^b_{ij} is the bond constant and b_{ij} is the bond length at equilibrium. In Fig. 2.5 the links correspond to bonds. Furthermore, the particles $\{2,3,4\}$ interact with each other via a harmonic angle potential, the Table 2.4 shows the definition of bonds. The bond angle potential is written as

$$V_{angle}(\theta_{ijk}) = \frac{1}{2}k^\theta_{ijk}\left(\theta_{ijk} - \theta^0_{ijk}\right)^2, \tag{2.15}$$

where Table 2.5 is the definition of the angle potential. Additionally, the complex of atoms in Fig. 2.5 has an extra torsion term over ϕ. This term has a similar format as previous harmonic terms,

$$V_{torsion}(\theta_{ijk}) = \frac{1}{2}k^\phi_{ijk}\left(\phi_{ijk} - \phi^0_{ijk}\right)^2. \tag{2.16}$$

These are the potentials that we have used in the case of simple molecules. Here, we use only the potential of *bond* and *angle*. However, molecules composed of many atoms are more complex. The dynamical description in this case requires more terms. Given the simplistic model in Fig. 2.5, the potential energy is described uniquely way via the pairs $\{k^b_{ij}, b_{ij}\}$, $\{k^\theta_{ij}, \theta^0_{ij}\}$ and $\{k^\phi_{ij}, \phi^0_{ij}\}$. There are physical systems that are described by different molecules. In this case, we need to define each group of molecules.

Figure 2.6 2D representation of the acetonitrile.

GROMACS & `moleculetype.itp`

First, we define the molecules. The `moleculetype.itp` file has the form:

Table 2.2 Type of molecule (i.e. CCN)

[moleculetype]	
Name	*nrexcl*
CCN	3

Table 2.2 shows as an example, where $nrexcl = 3$ refers to non-bonded interactions that have been excluded between atoms no further than 3 bonds away.

Table 2.3 Atoms parts of the molecule

[atoms]							
number[simplicity]	*type[atomtype.itp]*	*resnr*	*resid*	*atom*	*cgnr*	*charge*	*mass*
1	N1	1	CCN	N1	1	-0.5126	14.0067
2	C1	1	CCN	C1	2	0.4917	12.0110
3	C2	1	CCN	C2	3	-0.5503	12.0110
4	H21	1	CCN	H21	4	0.1904	1.0080
5	H22	1	CCN	H22	5	0.1904	1.0080
6	H23	1	CCN	H23	6	0.1904	1.0080

Here, it is useful to distinguish the difference between *atomtypes* (second column) and *atoms* (fifth column) in the Table 2.1. The *type* column is the atom type as defined in the previous section `atomtype.itp`. Instead, the *atom* contains the atom names of the simulated system (in our case are the same). The *cgnr* corresponds to the charge group number, so here each atom defines a unique group.

The function type defines the specific type of bonds. Here we use the harmonic type potential for bonds and by definition, it takes the value 1. In the same way the angles are defined see Table 2.5.

Table 2.4 Bonds

[bonds] *atom i*	*atom j*	*func. type*	$b_{ij}^{0}[nm]$	$k_{ij}^{b}[kJ\ mol^{-1}\ nm^{-2}]$
1	2	1	0.11570	502080.0
2	3	1	0.14580	334720.0
3	4	1	0.10900	284512.0
3	5	1	0.10900	284512.0
3	5	1	0.10900	284512.0

Table 2.5 Angles

[angles] *atom i*	*atom j*	*atom k*	*func. type*	$\theta_{ijk}^{0}[degree]$	$k_{ij}^{\theta}[kJ\ mol^{-1}\ rad^{-2}]$
1	2	3	1	180.000	669.44
2	3	4	1	110.000	669.44
2	3	5	1	110.000	292.88
2	3	6	1	110.000	292.88
4	3	5	1	109.500	292.88
4	3	6	1	109.500	292.88
5	3	6	1	109.500	292.88

2.4 System: atoms and molecules

The potential energy has been set up. Next, we must combine the potential energy information describing the simulations box. This procedure in the GROMACS community is called *topology*. This file contains the total description of the potential energy of the simulated system regarding inter-molecular and intra-molecular interactions.

GROMACS and topol.top

The default section is the description of the non-bonded interactions. Until this point, the potential or configuration energy is well described. However, the interactions between atoms and molecules can be parametrized further, and this is the essential idea of the force field parameterization and the development of different force fields for different molecular systems. Here, the *nbfunc=1* refers to the Lennard-Jones interactions where *comb-rule* is the Lorentz-Berthelot [23] combination rule. The *fudgeLJ* and *fudgeQQ* are factors multipliers of (1-4) pairs in the case of Lennard-Jones and Coulomb interactions, respectively. The specific [defaults] section on Table 2.6 is an AMBER-based [24] force field like the dynamic parameters that we implemented.

Based on Fig. 2.7, the bonded interactions of the system are written as

Table 2.6 Force field file

[defaults]				
nbfunc	*comb-rule*	*gen-pairs*	*fudgeLJ*	*fudgeQQ*
1	2	yes	0.5	0.8333

#include "atomtypes.itp"
#include "ccn.itp"

[system]
Neat acetonitrile

[molecules]
CCN 1462

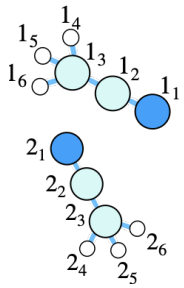

Figure 2.7 Example of interactions based on two CCN molecules.

$$U_{bonded}(r,\theta) = \sum_{i=1}^{2}\sum_{k=1}^{6} \underbrace{H_{i_k}(r,\theta)}_{moleculetype.itp} \quad , \tag{2.17}$$

and the non-bonded terms are:

$$U_{non-bonded}(r) = \sum_{k=1}^{6} \underbrace{H_{1_k 2_k}(r) + H_{1_1 1_4}(r) + \ldots}_{atomtype.itp}. \tag{2.18}$$

Now, by implementing the `topol.top` we add extra constraints to the total potential energy, for instance, the cancellation of the LJ interactions of the interatomic pairs on the acetonitrile molecule considering the *pairs* defined in `moleculetype.itp`. Additionally, the Lorentz-Berthelot rule is applied.

2.4.1 Non-bonded interactions scaling and exclusion.

The non-bonded interactions are written using the AMBER-based force field [24] representation. By implementing the *topol.top* eq. 2.18 is written as

$$U^{6-12}_{non-bonded}(r) = \sum_{k=1}^{6} \underbrace{H^{Lorentz-Berthelot}_{1_k 2_k}(r)}_{atomtype.itp}. \tag{2.19}$$

The electrostatic interactions have a special treatment, and we will present a detailed description of electrostatics in molecular dynamics simulations in Chapter 3. In the case of AMBER-based force fields, there are scaling corrections for the 1-4 pair interactions i.e in Fig. 2.7 $\{1_1 - 1_4\}$, $\{1_1 - 1_5\}$ and $\{1_1 - 1_6\}$. The non-bonded interactions for these pairs are given by

$$U^{(1-4)}_{LJ}(r) = fudgeLJ \cdot \sum_{i=1}^{2} \sum_{k,l} \underbrace{H^{Lorentz-Berthelot}_{i_k i_l}(r)}_{atomtype.itp}, \tag{2.20}$$

$$U^{(1-4)}_{electrostatics}(r) = fudgeQQ \cdot \sum_{i} \sum_{j \neq i} \underbrace{U^{ij}_{electrostatics}(r)}_{see\ Chapter\ 3}. \tag{2.21}$$

The non-bonded pair interactions (1-2) and (1-3) have been omitted. The interaction potential for our simplistic system is then given by.

$$U_{tot}(r,\theta) = U_{bonded}(r,\theta) + U_{LJ}(r) + U_{electrostatics}(r) + U^{(1-4)}_{LJ}(r) + U^{(1-4)}_{electrostatics}(r). \tag{2.22}$$

2.4.2 Radius cut-off

The computation of the interactions is a computationally time-consuming process. To make the molecular dynamics simulations much more efficient we introduce a cut-off radius r_{LJ}. We choose a $r_{LJ} = 1.4\ nm$ where $U_{LJ}(r > r_{LJ}) = 0$. This approach can be applied since the Lennard-Jones potential behaves as $1/r^6$ for larger values of r. Furthermore, electrostatics are long-range interactions, $1/r$, an electrostatic cut-off radius ($r_{el.}$) will accelerate the computations. However, such a choice will introduce artefacts [25] affecting the electrostatics of a bulk system, producing the wrong evaluation of the system's dynamics, resulting in a collection of microstates (a trajectory) that does not represent the right physical description. A detailed analysis of the electrostatic interaction treatment is given in Chapter 3.

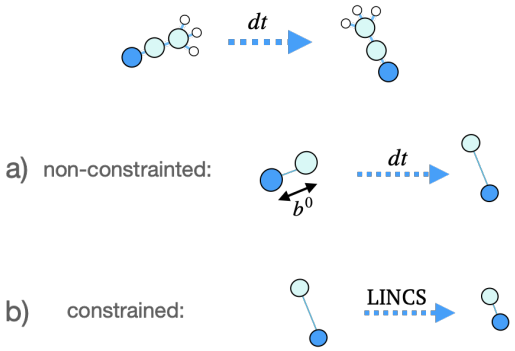

Figure 2.8 An illustration of the constraint algorithm. Resetting the constraints after the unconstrained behavior.

2.4.3 LINCS

As mentioned previously, the covalent bonds between atoms are determined as oscillators. These are high-frequency oscillations with low amplitude. An efficient way to deal with the behavior of bond vibrations is to consider constraints that are almost exclusively in their vibrational ground state. A detailed algorithm review can be found in the original work [26]. A schematic representation of the constrained algorithm is given in Fig.2.8. The LINCS algorithm is applied to the case of big (or small) molecules but not to water molecules by default. Finally, this algorithm has proven to be *symplectic*, preserving the accuracy of solving the equations of motion as discussed in the next section.

2.5 Water molecules

Water is a paradigmatic molecule. Its physical and chemical properties are unique and have many implications in our lives. Water is a special subject of study by itself and here we focus on its molecular dynamical description using molecular dynamic simulations. As we mentioned earlier, for the force field implementation the electrostatic interaction model that we consider employs only charges. This model for water molecules is called the simple point-charge model (SPC) [27].

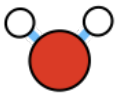

Figure 2.9 Water molecule, where red corresponds to the oxygen atom and the white circles represent the hydrogen atoms connected to the oxygen atom via hydrogen bonds.

An adequate, an effective potential description of the force field is demanding, as such the induced dipole moment should be considered. Consider a system of permanent charges and induced dipoles q_i and μ_i accordingly. The interaction model in MD simulations employs only charges. In the SPC/E [28] water model, the induced moments have been incorporated into the fixed charges. Hence, the permanent dipole of isolated water is renormalized. The potential V_i at the charges is given by

$$V_i = \sum_{i \neq j} \left[\frac{q_j}{r_{ij}} + \mathbf{G}\left(\mathbf{r}_{ij}\right) \mu_i \right], \tag{2.23}$$

where

$$\mathbf{G}(\mathbf{r}) = \frac{\mathbf{r}}{r^3}, \tag{2.24}$$

and the induced dipoles

$$\mu_i = \alpha_i \mathbf{E}_i, \tag{2.25}$$

where α_i is the polarizability and

$$\mathbf{E}_i = \sum_{i \neq j} \left[\mathbf{G}(\mathbf{r}_{ij}) q_j + \mathbf{T}\left(\mathbf{r}_{ij}\right) \mu_i \right], \tag{2.26}$$

where

$$\mathbf{T}(\mathbf{r}) = \frac{3\mathbf{r}\mathbf{r} - \mathbf{1}r^2}{r^3} \tag{2.27}$$

Eq. 2.24-2.27 can be solved for the induced dipoles. Note that here the total potential energy of the system in the SPC/E model is given by

$$U = \sum_i \int_0^1 \lambda V_i q_i d\lambda = \frac{1}{2} \sum_i q_i V_i. \tag{2.28}$$

If the induced dipoles were explicitly treated, the electrostatic interaction would be written as

$$E_{el} = \frac{1}{2} \sum_i q_i V_i - \frac{1}{2} \sum_i \mu_i \mathbf{E}_i. \tag{2.29}$$

Rewriting eq. 2.28

$$U = E_{el} + \underbrace{\frac{1}{2}\sum_i \mu_i^2/\alpha_i}_{\textit{polarized state cost}} \quad . \tag{2.30}$$

Thus

$$\langle \mu_i^2 \rangle = \langle \mu_i \rangle^2, \tag{2.31}$$

and the polarized term,

$$\langle E_{pol} \rangle = \frac{1}{2}\sum_i \langle \mu_i \rangle^2/\alpha_i. \tag{2.32}$$

In this case, the effective pair potential can be written using the following polarization correction

$$E_{pol} = \frac{1}{2}\sum_i \left(\mu - \mu^0\right)^2/a_i, \tag{2.33}$$

where μ is the dipole moment of the effective pair model and μ^0 is the dipole moment of the isolated molecule. The correction of eq. 2.33 has been done by the work of [28] by increasing the charge of the SPC model. Finally, the TIP4P water model consists of three fixed point charges and one Lennard-Jones center and it gives good predictions of density for values in temperature and pressure [29]. Both the SPC and TIP4P water models have been applied to describe the water and acetonitrile mixtures.

Summary

Here, we defined the main ingredients of a molecular system, such as atoms and molecules, using computer simulations. Then, we explain the idea of force field as a way of describing the interactions between the particles. It contains the potential energy information of a many-body classical system of particles. Finally, these are integrated by Newton's law based on the ergodic principle of statistical mechanics obtaining different thermodynamics ensembles.

Chapter 3

Electrostatics & Molecular Dynamics Simulations

The calculation of electrostatic interactions is a challenging computational task and needs special treatment during molecular dynamics simulations. In this chapter, we plan to give an overview of the different techniques for treatment and the importance of the boundary conditions. The most common boundary conditions in computer simulations are the periodic boundary conditions (PBC). Fig. 3.1 shows a PBC two-dimensional representation

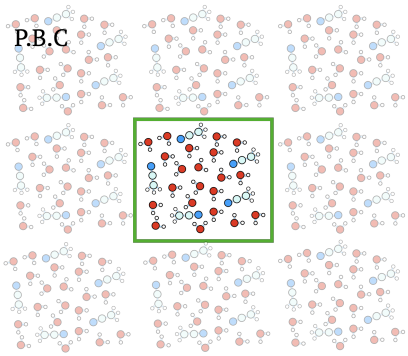

Figure 3.1 The simulation box (or super-cell) in green with its periodic replica images in fading colors

In general, the potential energy of a system of N particles with interaction potential $\phi(\mathbf{r}_{ij})$ under PBC is written as:

$$U(\mathbf{r}) = \frac{1}{2}\sum_{\mathbf{n}}\left[\sum_{i=1}^{N}\sum_{j=1}^{N}\phi(\mathbf{r}_{ij}+L\mathbf{n})\right], \tag{3.1}$$

with $\mathbf{n}$: *the number of cells*. Some of the possible interactions ϕ that govern a Coulomb system are

$$\begin{aligned}
\phi_{c.c.}(\mathbf{r}) &= q_i q_j |\mathbf{r}_{ij}|^{-1}, && (3.2)\\
\phi_{c.d.}(\mathbf{r}) &= -q_i \boldsymbol{\mu}_j \nabla(1/|\mathbf{r}_{ij}|), && (3.3)\\
\phi_{d.d.}(\mathbf{r}) &= -(\boldsymbol{\mu}_i \nabla)(\boldsymbol{\mu}_j \nabla)(1/|\mathbf{r}_{ij}|), && (3.4)\\
\phi_{c.q.}(\mathbf{r}) &= -q_i \mathbf{K}_j : \nabla\nabla(1/|\mathbf{r}_{ij}|)., && (3.5)
\end{aligned}$$

where q_i is the charge of atom i, $\boldsymbol{\mu}_i = \sum_i q_i \mathbf{r}_i$ the dipole moment of molecule i and $\mathbf{K}_i = \sum_\alpha q_\alpha (\mathbf{r}_{i\alpha} - \mathbf{R_i})(\mathbf{r}_{i\alpha} - \mathbf{R_i}) + (\text{const})\mathbf{I}$, with ':' denotes the colon operator. The pairs of interactions i.e. "*c.c.*" referred to charge-charge interactions with "*d*" for dipoles and with "*q*" quadrupoles correspondingly. In molecular dynamics, simulations have been considering only the charge-charge interaction except a few of the simulations [30]. A Coulomb system in PBC was introduced by *de Leeuw et al.* [31]. Eq. 3.1 is a series and its convergence is physically meaningful. In the case of "*charge-charge*" interaction $\phi_{c.c.}$ eq. 3.1 converges conditionally (considering a convergence factor for spherical shells) if charge neutrality holds. As $|\mathbf{n}| \to \infty$ the lattice sum terms are $\mathscr{O}\left(|\mathbf{n}|^{-3}\right)$ [32]. The total electrostatic energy considering only the charge-charge interaction for a cubic lattice of unit spacing for spherical shells is given by

$$H = \sum_{1 \le i < j \le N} q_i q_j \psi(\mathbf{r}_{ij}) + \frac{1}{2}\xi \sum_i^N q_i^2 + \frac{2\pi}{3}\left\|\sum_{i=1}^N q_i \mathbf{r}_i\right\|^2, \tag{3.6}$$

where

$$\psi(\mathbf{r}) = \sum_{\mathbf{n}} \frac{erfc(\alpha|\mathbf{r}+\mathbf{n}|)}{|\mathbf{r}+\mathbf{n}|} + \frac{1}{\pi}\sum_{\mathbf{n}\neq 0} |\mathbf{n}|^2 \exp\left[2\pi i \mathbf{n}\cdot\mathbf{r} - \pi^2 |\mathbf{n}|^2/\alpha^2\right], \tag{3.7}$$

in which

$$erfc = 1 - 2\pi^{-1/2}\int_0^\pi e^{-t^2} dt \tag{3.8}$$

is the complementary error function and

$$\xi = \sum_{\mathbf{n}\neq 0}\left[\frac{erfc(\alpha|\mathbf{n}|)}{|\mathbf{n}|} + \frac{1}{\pi|\mathbf{n}|^2} e^{-\pi^{2}\mathbf{n}^2/\alpha^2}\right] - \frac{2\alpha}{\pi^{1/2}}. \tag{3.9}$$

Eq. 3.9 can be then written as

$$\xi = \lim_{|\mathbf{r}|\to 0}\left[\psi(\mathbf{r}) - |\mathbf{r}|^{-1}\right]. \tag{3.10}$$

However, if the total electric moment, $\mathbf{M} = \sum_i^N q_i \mathbf{r}_i$, is zero, then the series are absolutely convergent ($\mathscr{O}\left(|\mathbf{n}|^{-5}\right)$ for $|\mathbf{n}| \to \infty$) which means the summation of the electrostatic interactions do not depend on the *geometry*. The way that we sum up and the boundary conditions that have been applied are called *geometry*. The last term of eq. 3.6 is called the surface term and depends on how we sum up the electrostatic interactions. The corresponding *geometry* has been introduced in [31] by the convergence factors associated with the electrostatics of continuum bodies.

Eq. 3.6 is enough to describe the physical behavior in molecular dynamics simulations, as it has been reported in the case of non-polarized systems. The effect of the extra multipole components appears to be zero in the thermodynamic limit [31]. Although, eq. 3.6 can be written in a more generalized way of a sphere inside a dielectric medium ε' [33, 34], with the electrostatic energy,

$$H = H^{(r)} + H^{(k)} + H^{(s)} + H^{(d)}, \tag{3.11}$$

written in terms of real space (r), reciprocal space (k), self-term (s), and surface contributions (d).

$$H^{(r)} = \frac{1}{2}\sum_{i\neq j}\sum_{\mathbf{n}\in Z^3} q_i q_j \frac{erfc\left(\alpha\left|\mathbf{r}_{ij}+\mathbf{n}L\right|\right)}{\left|\mathbf{r}_{ij}+\mathbf{n}L\right|}, \tag{3.12}$$

$$H^{(k)} = \frac{1}{2L^3}\sum_{\mathbf{k}\neq 0}\frac{4\pi}{k^2}\exp^{-k^2/4\alpha^2}\left|\rho(\mathbf{k})\right|^2, \tag{3.13}$$

$$H^{(s)} = -\frac{\alpha}{\sqrt{\pi}}\sum_i q_i^2, \tag{3.14}$$

$$H^{(d)} = \frac{2\pi}{(1+2\varepsilon')L^3}\left(\sum_i q_i \mathbf{r}_i\right)^2, \tag{3.15}$$

with $\tilde{\rho}(\mathbf{k}) = \int_{V_b} d\mathbf{r}\rho(\mathbf{r})e^{-i\mathbf{kr}} = \sum_{j=1}^N q_j e^{-i\mathbf{kr}_j}$ and α a weight relation of the real and reciprocal space. L is the simulation box length. Omitting the surface term in eq. 3.15 corresponds to the well-known *tin-foil* boundary conditions ($\varepsilon' \to \infty$).

3.1 Electrostatics without a "mesh"

Here, we will present a simple theoretical calculation for a periodic replication of a water molecule. This section presents the computational implementation of the electrostatic interactions in the case of a simple system such as a water molecule and its replicas.

We can solve Poisson's equation for the electrostatic potential Φ for a charge density ρ_q.

$$\nabla^2\Phi = -4\pi\rho_q. \tag{3.16}$$

This problem has to be solved in the case of a finite system with periodic boundary conditions. Thus, a Green function $G(\mathbf{r})$ contains the dynamical information (propagates the particle interaction) which can be used to solve eq. 3.16 straightforward,

$$\Phi(\mathbf{r}) = \int_{\Omega} d\mathbf{r}' G\left(\mathbf{r}-\mathbf{r}'\right)\rho_q(\mathbf{r}'), \tag{3.17}$$

where Ω is the box size. Here, we will present the Ewald summation and the calculation of eq. 3.17 in the case of a water molecule. The charge density distribution using the delta function $\delta(\mathbf{r})$ to describe the local character of a point charge distribution, is written as:

$$\rho_q(\mathbf{r}') = q_O\delta(\mathbf{r}'-\mathbf{r}_O) + q_{H_1}\delta(\mathbf{r}'-\mathbf{r}_{H_1}) + q_{H_2}\delta(\mathbf{r}'-\mathbf{r}_{H_2}). \tag{3.18}$$

By substituting eq. 3.18 into eq. 3.17, the electrostatic potential for a water molecule is

$$\Phi(\mathbf{r}) = q_O G(\mathbf{r}-\mathbf{r}_O) + q_{H_1} G(\mathbf{r}-\mathbf{r}_{H_1}) + q_{H_2} G(\mathbf{r}-\mathbf{r}_{H_2}) \tag{3.19}$$

and the Ewald summation for choosing a proper α is written as

$$G(\mathbf{r}) = \Theta(r_c-r)\frac{erfc(\alpha r)}{r} - \frac{\pi}{\alpha^2 V} + \frac{1}{V}\sum_{\mathbf{k}\neq 0}\frac{4\pi}{k^2}e^{-\frac{k^2}{4\alpha^2}}e^{i\mathbf{kr}}. \tag{3.20}$$

Finally, the potential of a water molecule in periodic boundary conditions is given by eq. 3.19 (see Fig. 3.2). Now, it is crucial to understand what we have achieved. The electrostatic potential can be used to derive the electrostatic field and corresponding electrostatic force acting on a particle.

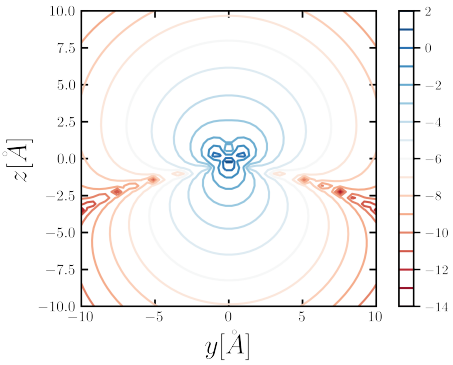

Figure 3.2 The electric potential of a water molecule in a simulation box with $L = 3.6\,nm$. The contour plot is on a logarithmic scale of the absolute field value ($log(|\phi(\mathbf{r})|)$). The grid on the $k-space$ is made by 13^3 collections each for k_+ and k_-. The space discretization was based on a grid $\{x,y\} \in [-10,10]$ with a spacegrid of 0.2. The water molecule atom coordinates are: $\mathbf{r}_O = (0,0,-0.289)$, $\mathbf{r}_{H_1} = (0,0.816,0.289)$ and $\mathbf{r}_{H_2} = (0,-0.816,0.289)$. Our derivation seems to be in agreement with [35]. The author would like to acknowledge Dr. Peter Wirnsberger for a useful discussion on this plot.

3.2 Reaction field & surface terms

3.2.1 Reaction field

The electrostatic interaction of a simulation box can also be computed without using any periodic image conditions. This method, called reaction field treatment [36], is consistent with the continuum dielectric theory (see section 3.4). In the reaction field method, any molecular dipole μ_i is at the center of a cutoff sphere of radius r_c, which is surrounded by a dielectric continuum of permittivity ε_{RF}. The electrostatic energy has an additional term,

$$U_{RF} = -\frac{1}{2}\frac{\varepsilon_{RF}-1}{\varepsilon_{RF}+\frac{1}{2}}\frac{1}{r_c^3}\sum_i \mu_i \cdot \mathbf{M}_i, \tag{3.21}$$

with $\mathbf{M}_i$ being the total dipole moment of the spherical cavity. Now, if we consider eq. 3.21 in the case where $r_c^3 = \frac{3}{4\pi}v_{cube}$ and the dipole moment for strict minimum image truncation is constant, then the last term of eq. 3.21 is written as:

$$\sum_i \mu_i \cdot \mathbf{M}_i = \mathbf{M}_i \sum_i \mu_i = \mathbf{M}^2 = \left(\sum_i q_i \mathbf{r}_i\right)^2. \tag{3.22}$$

This is equivalent to a cubic truncation geometry and for a dielectric constant of the surrounding medium of $\varepsilon_{RF} = \infty$ with $E_{depolorization} = -\frac{2\pi}{3u}\left(\sum_i q_i \mathbf{r}_i\right)^2$. The reaction field method introduces some artefacts causing the system's energy drift. Considering, that an

r_c corresponds to a dipole sphere around a molecule. As the system evolves in time, each sphere exchanges molecules with each other, increasing each molecule's kinetics since it responds with a different dipole sphere each time. This phenomenon can be smoothed using a tapering radius r_T and employing spline functions ($f_T(r_{ij})$) [37]. At the end, the cubic cutoff electrostatic is summarized as:

$$U_E(r_{ij}) = \begin{cases} U_{q_iq_j}(r_{ij}) + U_{RF} & r_{ij} \leq r_T \\ U_{q_iq_j}(r_{ij}) + f_T(r_{ij})U_{RF} & r_T \leq r_{ij} \leq r_c, \\ 0 & r_{ij} \geq r_c \end{cases} \tag{3.23}$$

where U_{RF} is given by eq. 3.21 and $U_{q_iq_j}(r_{ij})$ is the potential given by eq. 3.2.

3.2.2 Surface term $J(\mathbf{M},\mathbf{S})$

The surface term for spheres by a continuum of dielectric constant ε' is given by eq. 3.15 where $\mathbf{M} = \sum_i q_i \mathbf{r}_i$ is the total dipole moment of the simulation box. The definition with the case of ionic-free solutions. However, eq. 3.15 is not consistent for ionic solutions. The reason is that we need to consider a consistent frame of reference for computing the polarization. The generalization of the surface term in molecular dynamics for surrounding spherical cells is written as:

$$J(\mathbf{M},S) = \frac{2\pi}{V}\frac{1}{2\varepsilon'+1}\mathbf{M}_i^2, \tag{3.24}$$

where now $\mathbf{M}_i$ is the itinerant polarization and V denotes the system's volume. $\mathbf{M}_i$ is defined as the electric moment of the charges that were in the supercell $\mathscr{C}$ ($\mathbf{n} = 0$) at $t = 0$ and may have diffused away in the neighboring cells ($\mathbf{n}$ cells) in the course of calculation.

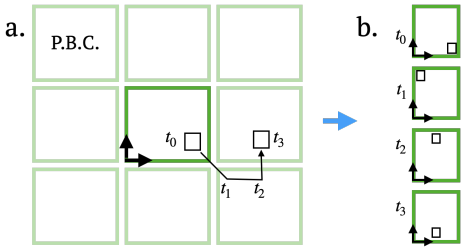

Figure 3.3 a. Unwrapped representation of the coordinates and b. Wrapped transformation. In the case of an ionic solution, the polarization should be calculated using the unwrapped coordinates at each time step.

However, in the case of polar non-ionic solutions, the *itinerant* and *bulk* polarizations are equal $\mathbf{M}_i = \mathbf{M}_B$. The consideration of the *itinerant* polarization framework is not a matter

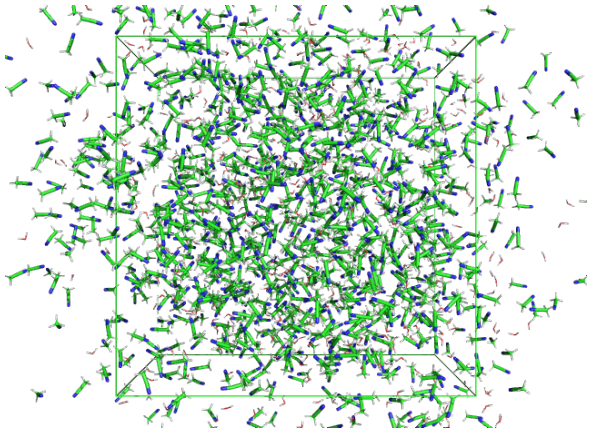

Figure 3.4 The unwrapped three-dimensional representation of water and acetonitrile simulation box.

of "taste", but it corresponds to physically consistent results in the case of ionic solutions. Indeed, Stillinger-Lovett (SL) conditions [38] have been proven to be fulfilled in the case of an ionic solution by adapting the *itinerant* polarization framework [32]. Stillinger-Lovett's conditions express the fact that a conducting dielectric medium acts as a dielectric shield when a slow varying in space external electric field is applied [32].

In the case of non-conducting boundary conditions ($\varepsilon \neq \infty$), the electrostatic energy has an additional term. $J(\mathbf{M}, G)$ is a shape-dependent term and depends on the *geometry* G, as we mentioned in the introduction of this chapter. When spherical geometry is used for summation ($G = S$), the $J(\mathbf{M}, S)$ is given by

$$J(\mathbf{M}, S) = \frac{2\pi}{(2\varepsilon' + 1)V} |\mathbf{M}|^2, \tag{3.25}$$

with $\mathbf{M}$ the itinerant polarization of the simulation box [32]. The eq. 3.25 had been introduced by *De Leeuw and Parram* [39]. A derivation of eq. 3.25 can be obtained based on the theory of dielectric theory (see subsection 3.4.2). The calculation of the electrostatic force is always the same,

$$\Phi_{Ewald} \rightarrow \mathbf{E}_{Ewald} \rightarrow \mathbf{F}_{Ewald}, \tag{3.26}$$

and these interactions have been derived from the electrostatic potential Φ_{Ewald}. Now, the difference between the evolution of a system with tin-foil boundary conditions (or conducting boundary condition or Ewald-Kornfeld boundary conditions or $\varepsilon_S \rightarrow \infty$) and the case of insulating boundary conditions ($\varepsilon_S \rightarrow 0$) is an extra force term. In the case of systems with an additional surface term $J(\mathbf{M}, G = S)$, there is an additional force acting on the charged particles [40]

$$\mathbf{F}_i = -\nabla_i J(\mathbf{M}, S) = -\frac{4\pi q_i}{3V}\mathbf{M}, \tag{3.27}$$

The electrostatic energy derived from the Ewald summation is unique. The electrostatic energy of a unit cell can be written as follows [41]

$$U_{vacuum} = U_{Ewald} + U_{polarization}, \tag{3.28}$$

with $U_{polarization} = \frac{2\pi}{3v}\left(\sum_i q_i \mathbf{r}_i\right)^2$. Here $\mathbf{r}_i$ and q_i are the positions and charges of particles in a unit cell of volume v. In molecular simulations, we always consider a neutral unit cell ($\sum_i q_i = 0$). U_{vacuum} is nothing but the electrostatic energy of a system surrounded by empty space. Instead, U_{Ewald} corresponds to the same system immersed in a perfectly conducting medium that neutralizes all the surface charges (tin-foil boundary conditions).

At this point, two main methods of electrostatic treatments have been showed. Among the electrostatic treatments, the Ewald and Reaction field methods are the most popular in molecular dynamics simulations. We would like to discuss the implications of different boundary conditions and computational techniques accordingly.

- Ewald (Mesh techniques): $U_{Ewald} + J(\mathbf{M}, G)$
  - EW3D (*toroidal or sphere*)
    - *Vacuum*: $\varepsilon \to 1 \Rightarrow J(\mathbf{M}, G = S) = \frac{2\pi}{3V}|\mathbf{M}|^2$
    - *Tinfoil*: $\varepsilon \to \infty \Rightarrow J(\mathbf{M}, G = S) = 0$
  - EW3DC (*rectangular plate or disk*)
    - $J(\mathbf{M}, G = P) = \frac{2\pi}{V} M_z^2$, only for $\varepsilon' \to 1$
- Cubic cutoff (Reaction field): U_E
  - *Vacuum*: $\varepsilon_{RF} \to 1 \Rightarrow U_{RF} = 0$
  - *Tinfoil*: $\varepsilon_{RF} \to \infty \Rightarrow U_{RF} = -\frac{2\pi}{3u}\left(\sum_i q_i \mathbf{r}_i\right)^2$

The potential energy and the phase space landscape vary as a function of the *electrostatic treatment* and the *electrostatic boundary conditions* or *geometry*. These attributes have been classified in the seminal work of *Roberts and Schnitker* [41]. It is well known that the pair correlation functions are insensitive to the *electrostatic boundary conditions* but higher-order correlations are strongly influenced [31, 41]. As an example, the dielectric constant is a second-order correlation function. Consequently, the electrostatic boundary conditions are essential for the material's dielectric properties.

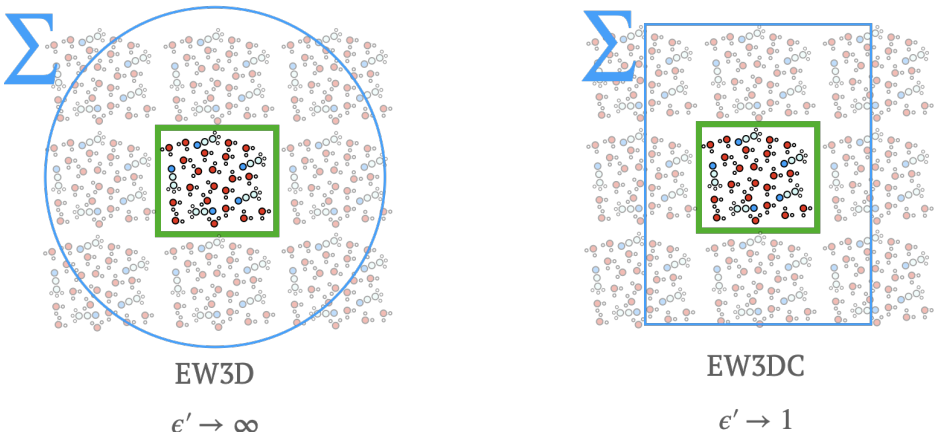

Figure 3.5 A schematic representation of the different Ewald geometries. Each sum denotes the summation geometry. In the case of EW3D, a spherical summation geometry has been used; thus we have the Ewald summation with a Hamiltonian description eq. 3.6. On the other hand, the well-known EW3DC method for application in slab systems is more complicated and can be described only for a system embedded in a dielectric continuum with $\varepsilon' \to 1$.

According to [41], as we go from *Ewald* to *Ewald + vacuum*, there is a virtual association with the *cubic cutoff* boundary conditions. However, this is invalid from the *cutoff + vacuum* to *cutoff + tinfoil* since the *Ewald* can not be recovered. This only applies to the *cubic cutoff + tinfoil* case. This problem is mainly dimensional (not finite size) and is related to the definition of the reaction field dielectric constant in finite systems. According to [41], the ε_{RF} is written as:

$$\frac{\varepsilon_{RF}-1}{\varepsilon_{RF}+\frac{1}{2}} = \frac{(L-r_T)^3}{L^3}. \tag{3.29}$$

Eq. 3.29 corresponds to the maximum value of $\varepsilon_{RF} \approx 50$ without reaching a conductor. Hence, there is an asymmetry of polarization and depolarization correction in the case of *cubic cutoff* (reaction field).

3.3 Particle mesh Ewald summation (PME)

3.3.1 Ewald summation

Here, we would like to present the technique to calculate the electrostatic interaction in eq. 3.13 under the particle mesh Ewald (PME) summation framework following the work of *Deserno et al.* [33]. To understand how the PME works, we start with the description of the electrostatics in the reciprocal space $H^{(k)}$ eq. 3.13.

$$H^{(k)} = \frac{1}{L^3} \sum_{\mathbf{k}\neq 0} \underbrace{\frac{4\pi}{k^2}}_{\tilde{g}(\mathbf{k})} \underbrace{\exp^{-k^2/4\alpha^2}}_{\tilde{\gamma}(\mathbf{k})} \tilde{\rho}(\mathbf{k}) \sum_{j=1}^{N} q_j e^{i\mathbf{k}\mathbf{r}_j}, \tag{3.30}$$

then eq. 3.30 can be written as

$$\begin{aligned} H^{(k)} &= \frac{1}{2} \sum_j q_j \left(\frac{1}{L^3} \sum_{\mathbf{k}\neq 0} \tilde{g}(\mathbf{k}) \tilde{\gamma}(\mathbf{k}) \tilde{\rho}(\mathbf{k}) e^{i\mathbf{k}\mathbf{r}_j} \right) \\ &= \frac{1}{2} \sum_j q_j \phi^{(k)}(\mathbf{r}_j). \end{aligned} \tag{3.31}$$

The physical meaning of eq. 3.31 corresponds to the distribution of charges on the simulation box in the real space. The electrostatic potential in the reciprocal space is written

$$\tilde{\phi}^{(k)}(\mathbf{k}) = \tilde{g}(\mathbf{k}) \tilde{\gamma}(\mathbf{k}) \tilde{\rho}(\mathbf{k}) \tag{3.32}$$

The $\gamma(\mathbf{k})$ is a consequence of the splitting function f. Eqs 3.12-3.15 have been introduced after rewriting the electrostatic interaction term $1/r$ as

$$\frac{1}{r} = \frac{f}{r} + \frac{1-f}{r}, \tag{3.33}$$

in this case, the splitting function is the complementary error function

$$erfc := \frac{2}{\sqrt{\pi}} \int_r^{\infty} e^{-t^2} dt. \tag{3.34}$$

The advantage of splitting the electrostatic interactions eq. 3.33 is due to the way the two parts are converging and considering the first term computing its contribution on the real space inside a sphere of radius r_{cutoff} where r_{cutoff} is smaller than the length of the simulation box L (see Fig. 3.6), then the first term converges fast. The second term is a slowly varying function in the real space. However, its Fourier expansion to reciprocal space converges fast.

Although, the real cutoff, which was introduced, causes some errors. Consider the following: we split the electrostatic potential in a specific radius cutoff, from that point and after, the contribution of the electrostatics have been computed by using the reciprocal space. This is equivalent to splitting the charge density instead of splitting the potential. We could imagine that, as the effect of f function as real cutoff r_{cutoff} causing a "blare" (or smearing) distribution of charges, which next corresponds to a grid-based charge density (mesh). A schematic representation is given in Fig. 3.7. At this point, we need to be careful as the

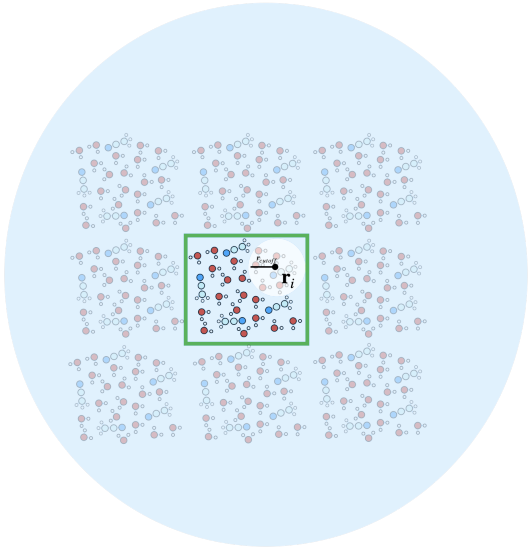

Figure 3.6 The simulation box in green with its periodic replicas images. A real cutoff, r_{cutoff}, has been introduced.

charge of a particle "splits into the mesh points". How to mesh up Ewald sums depends on the simulation method that has been used (see Fig. 3.8). For instance, Monte Carlo simulations require high accuracy regarding the energy, while molecular dynamics simulations are based on force accuracy.

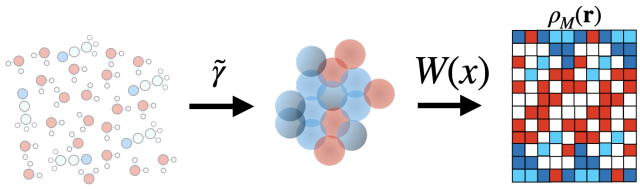

Figure 3.7 Interpretation of mesh or grid-based charge density referring to the treatment of the Fourier space component (second term of eq.3.33) where it has been applied for $r > r_{cut-off}$. The mesh method schemes use different charge assignment functions $W(x)$.

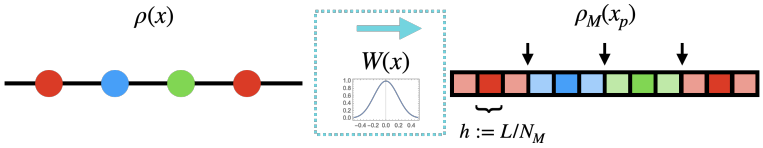

Figure 3.8 Illustration of charge assignment in 1D. On the left-hand side is the distribution of charges in real space. A proper selection of the $W(x)$ assigns the charges on the mesh. The vector sign on the right-hand side describes the areas where the method could cause artefacts/errors, and these are canceled or are zero in the backpropagation to the real space. This is an example with $h = 1/3$ and $P = 7$ (assignment scheme) $N_M = 12$ mesh points.

3.3.2 PME

As we mentioned before, the alignment of the charge on a mesh is crucial; the P.M.E is a finite Fourier transform of the mesh-based charge density.

$$\hat{\rho}_M(\mathbf{k}) := h^3 \sum_{\mathbf{r}_p \in \mathscr{M}} \rho_M(\mathbf{r}_p) e^{-i\mathbf{k}\cdot\mathbf{r}_p} \tag{3.35}$$

where $\sum_{\mathbf{r}_p \in \mathscr{M}}$ is the sum over the mesh in real space and $\mathbf{k}$-vectors correspond to the mesh Fourier space, h^3 denotes the element mesh-space volume (see Fig. 3.8).

Let us now analyze the electrostatics on the mesh. The total electrostatic energy on the mesh should be written as

$$H_{mesh} = \frac{1}{2} \sum_{\mathbf{r}_p \in \mathscr{M}} \rho_M(\mathbf{r}_p) \phi(\mathbf{r}_p) \tag{3.36}$$

Following the eqs. 3.32, 3.31, we can write

$$\phi(\mathbf{r}_p) = h^3 \sum_{\mathbf{r}_q \in \mathscr{M}} \rho_M(\mathbf{r}_q) G(\mathbf{r}_q - \mathbf{r}_p) \tag{3.37}$$

or as a finite convolution

$$[\rho_M \star G](\mathbf{r}_p) = h^3 \sum_{\mathbf{r}_q \in M} \rho_M(\mathbf{r}_q) G(\mathbf{r}_p - \mathbf{r}_q) \tag{3.38}$$

The function G is crucial since it contains the interaction information on the mesh. So, a proper G function should contain the information of the electrostatic interaction and the distribution of the γ smeared distribution. Indeed, the G in Fourier space can be written as

$$\hat{G}(\mathbf{k}) = B(\mathbf{k}) \sum_{\mathbf{m} \in Z^3} \frac{4\pi}{\left(\mathbf{k} + \frac{2\pi}{h}\mathbf{m}\right)^2} \tilde{\gamma}\left(\mathbf{k} + \frac{2\pi}{h}\mathbf{m}\right) \tag{3.39}$$

with $B(\mathbf{k}) := \left| b(k_x) b(k_y) b(k_z) \right|^2$. However, we want to achieve that

$$H^{(k)} \approx H_{mesh}. \tag{3.40}$$

For eq. 3.40 to remain valid we need to carefully construct a G function reducing the error between the continuum and mesh electrostatic assignment. This is the key critical difference for the different mesh Ewald schemes. Finally, we can write,

$$H^{(k)} \approx \frac{1}{2} \sum_{\mathbf{r}_p \in M} h^3 \rho_M(\mathbf{r}_p) [\rho_M \star G](\mathbf{r}_p) \tag{3.41}$$

Where we have the following quantities:

$$[\rho_M \star G](\mathbf{r}_p) \rightarrow \textit{potential energy of the meshed charge distribution via the Green function.} \tag{3.42}$$

and

$$\sum \rho_M [\rho_M \star G](\mathbf{r}_p) \rightarrow \textit{electrostatic energy on the mesh.} \tag{3.43}$$

The PME technique uses the Lagrange interpolation scheme and the unchanged Coulomb function with $B := 1$.

The implementation of the Ewald summations is the same in every scheme.

- calculate the mesh charge density ρ_M in Fourier space: $\hat{\rho}_M \rightarrow FFT[\rho_M]$
- calculate the influence function in the Fourier space: $\hat{G} \rightarrow FFT[G]$
- and finally: $\rho_M \star G = FFT^{-1}\left[\hat{\rho}_M \times \hat{G}\right]$

Force calculations on the mesh

The idea is to calculate the mesh-based electrostatic potential $\phi^{(k)}(\mathbf{r}_p)$ using the mesh based electric field $\mathbf{E}(\mathbf{r}_p)$

$$\begin{aligned}
\mathbf{E}(\mathbf{r_p}) &= -\frac{\partial}{\partial \mathbf{r}_p}\phi^{(k)}(\mathbf{r}_p) \\
&= -\frac{\partial}{\partial \mathbf{r}_p}[\rho_M \star G](\mathbf{r}_p) \\
&= -\frac{\partial}{\partial \mathbf{r}_p}\left(FFT^{-1}\left[\hat{\rho}_M \times \hat{G}\right]\right) \\
&= -FFT^{-1}\left[i\mathbf{k} \times \hat{\rho}_M \times \hat{G}\right].
\end{aligned} \tag{3.44}$$

This method is an efficient way that leads to the most accurate force calculations.

Calculation of forces in real space

The calculation is similar to the charge assignment. The force on particle i is given by

$$\mathbf{F}_i = q_i \sum_{\mathbf{r}_p \in M} \mathbf{E}(\mathbf{r}_p) W(\mathbf{r}_i - \mathbf{r}_p). \tag{3.45}$$

This expression is straightforward, especially in the *PME* scheme, where $W(\mathbf{r_i} - \mathbf{r_p})$ is the charge assignment function (see Fig. 3.8). Specifically, eq. 3.45 is the electrostatic force contribution to the total force for solving the equations of motion.

3.3.3 The errors of the particle mesh Ewald

The mesh Ewald summation has errors. The errors are introduced due to the mesh interpretation.

$$\Delta F = \sqrt{\frac{1}{N}\sum_{i=1}^{N}\left(\mathbf{F}_i^{mesh} - \mathbf{F}_i^{exa}\right)^2}. \tag{3.46}$$

First, we should explain how the Ewald parameter α is related to the error in forces (see FIG. 3.9).

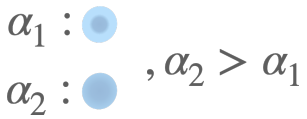

Figure 3.9 α: in the case of small and big values of α, the error is larger by the real space contribution and the Fourier contribution res§pectively. The α_1 represents a more point-like distribution, instead of the α_2 a more smeared-out distribution.

The minimum error occurs when the real space and Fourier space errors are equal. Deserno's work outputs that the *smooth particle mesh Ewald* $(SPME)$ [42] is 9.2 times more accurate than PME, while the *particle-particle-particle mesh Ewald* (P^3M) [43] is 33 times more accurate than PME. Additionally, the optimal value of α depends on the cutoff r_{max}. The decreased r_{max} corresponds to an increase in the real space contribution to the error.

3.4 Dielectric polarization & molecular dynamics simulations

A statistical calculation of the average local field in a molecule shows that fluctuations in the induced molecular moment give rise to a deviation from the Lorentz field.

Lorentz calculated the contribution to the internal field arising from the external sources and the polarization of the molecules outside the spherical surface of sufficient size to contain many molecules and concentric with the molecule, in which the field is desired. Onsager derived a more explicit description of the internal field [44]. The internal field can be decomposed into two fields: the *cavity field* **G** and the *reaction field* **R**. In an electric field **F**, the total electric moment is the vector sum of the permanent and induced dipole moments

$$\mathbf{m} = \mu_0 \mathbf{u} + \alpha \mathbf{F}, \tag{3.47}$$

where μ_0 is a permanent electric moment (*in vacuo*), and α is the polarizability.

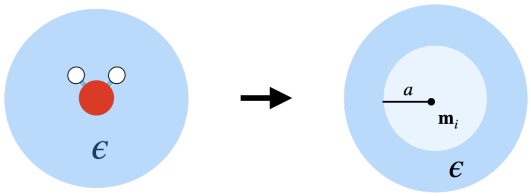

Figure 3.10 The Onsager's field representation.

For clarity, we consider an unpolarized medium of dielectric constant ε and introduce a rigid dipole moment m_i into a cavity of radius a see Fig. 3.10. This is a macroscopic representation since we try to compute the contribution to the internal field considering the dipolar representation of a water molecule (we have to zoom out with the radius a).

The potential ϕ has to satisfy the Laplace's equation:

$$\nabla^2 \phi = 0, \tag{3.48}$$

satisfying boundary conditions in polar coordinates

$$\psi(r,\theta) - \frac{\mathbf{m}_i cos\theta}{r^2} = continuous < \infty, \tag{3.49}$$

$$\left(\frac{\partial \psi}{\partial r}\right)_{r=a-\delta} = \varepsilon \left(\frac{\partial \psi}{\partial r}\right)_{r=a+\delta}. \tag{3.50}$$

The solutions in and out are written as:

$$\psi = \frac{m\cos\theta}{r^2} - Rr\cos\theta, (r < a), \tag{3.51}$$

$$\psi = \frac{m^*\cos\theta}{\varepsilon r^2}, (r > a), \tag{3.52}$$

where the coefficients m^* and R must equal

$$m^* = \frac{3\varepsilon}{2\varepsilon+1}m, \tag{3.53}$$

$$R = \frac{2(\varepsilon-1)}{2\varepsilon+1}\frac{m}{a^3}. \tag{3.54}$$

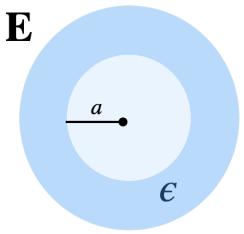

Figure 3.11 Empty cavity with an external electric field.

The modification of a homogeneous field **E** by an empty spherical cavity (Fig. 3.11) is given by

$$\psi(r,\theta) + Er\cos\theta = continuous < \infty, \tag{3.55}$$

with coefficients

$$M = \frac{\varepsilon-1}{2\varepsilon+1}Ea^3, \tag{3.56}$$

$$G = \frac{3\varepsilon}{2\varepsilon+1}E. \tag{3.57}$$

Inside the cavity, the total field, according to eq. 3.54 and eq. 3.57 is given by

$$\mathbf{F} = \mathbf{G} + \mathbf{R} = \frac{3\varepsilon}{2\varepsilon+1}\mathbf{E} + \frac{2(\varepsilon-1)}{(2\varepsilon+1)a^3}\mathbf{m} \tag{3.58}$$

Finally, the *reaction field* R (eq. 3.54) corresponds to an energy contribution U_{RF} given by eq. 3.21.

3.4.1 Dielectric susceptibility

Inside a dielectric cavity, its total dipole moment is defined by $\mathbf{M}$. The electric field inside the cavity is $\mathbf{E}_c$. The system's Hamiltonian is written

$$H = H_0 - \mathbf{M} \cdot \mathbf{E}_c, \tag{3.59}$$

with H_0 is the non-perturbative Hamiltonian and

$$\mathbf{M} = \sum_{i=1}^{N_0} \mathbf{m}_i, \tag{3.60}$$

with m_i the dipole moments inside the cavity.

In the absence of any dielectric and when the externally applied field is $\mathbf{E}'$, then $\mathbf{E}_c = \mathbf{E}'$, the usual boundary conditions of macroscopic electrostatics relate the two fields. Considering $\Delta\mathbf{E} = \mathbf{E}_c(r) - \mathbf{E}_c^0(r)$, the difference of the electric field inside due to the external field and all the dipoles ($\mathbf{E}_c(r)$), and the mean electric field when no external field is applied ($\mathbf{E}_c^0(r)$). Then the induced polarization can be written as:

$$\Delta\mathbf{P}(\mathbf{r}) = \frac{1}{4\pi} \int_{\mathscr{D}_{cavity}} \overline{x}(\mathbf{r}, \mathbf{r}') \Delta\mathbf{E}(\mathbf{r}') d\mathbf{r}'. \tag{3.61}$$

Eq. 3.61 can be simplified for slowly varying $\Delta\mathbf{E}(\mathbf{r})$ [45], the integral factorizes approximately and eq. 3.61 is now written as

$$\Delta\mathbf{P}(\mathbf{r}) = \frac{1}{4\pi} \overline{x}(\mathbf{r}) \Delta\mathbf{E}(\mathbf{r}). \tag{3.62}$$

At this point, we should consider how molecular dynamics simulations work with an external applied electric field $\mathbf{E}$. The cavity, in this case, is the entire simulation box. The local permittivity tensor is defined as

$$\overline{x}(\mathbf{r}) = \overline{\varepsilon}(\mathbf{r}) - \overline{I}. \tag{3.63}$$

Finally, the induced polarization can be written as

$$\Delta\mathbf{P}(\mathbf{r}) = \mathbf{P}(\mathbf{r}) - \mathbf{P}_0(\mathbf{r}) = \langle \mathbf{m}(\mathbf{r}) \rangle_{\mathbf{E}'} - \langle \mathbf{m}(\mathbf{r}) \rangle \tag{3.64}$$

$$= \frac{\int d\mathbf{r}_1 ... \int d\mathbf{r}_N \left[\mathbf{m}(\mathbf{r}) - \langle \mathbf{m}(\mathbf{r}) \rangle \right] \exp(-\beta H)}{\int d\mathbf{r}_1 ... \int d\mathbf{r}_N \exp(-\beta H)}. \tag{3.65}$$

Following the arguments of eq. 3.62 the eq. 3.65 is written after a linearization

$$\Delta P_i(\mathbf{r}) = \beta \sum_{j=x,y,z} \left[\left\langle m_i(\mathbf{r}) M_j \right\rangle - \left\langle m_i(\mathbf{r}) \right\rangle \left\langle M_j \right\rangle \right] \tag{3.66}$$

As we mentioned previously, the cavity field $\mathbf{E}_c$ and the external electric field $\mathbf{E}'$ are related according to eq. 3.57

$$\mathbf{E}_c = \frac{3\varepsilon'}{2\varepsilon'+1}\mathbf{E}', \tag{3.67}$$

where ε' refers to the surrounding dielectric medium. Furthermore, for spherical geometry, following the work of *Ballenegger and Hansen* [45] where the cavity is embedded in a dielectric medium with dielectric constant ε' the eq. 3.66 is written as

$$\frac{(\varepsilon-1)(2\varepsilon'+1)}{(2\varepsilon'+\varepsilon)} = \frac{4\pi\varepsilon}{3}\left[\langle \mathbf{m}(\mathbf{r})\mathbf{M}(\mathbf{r})\rangle - \langle \mathbf{m}(\mathbf{r})\rangle \langle \mathbf{M}(\mathbf{r})\rangle\right], \tag{3.68}$$

in the limit $\varepsilon' \to \infty$ eq. 3.68 is written as

$$\frac{\varepsilon-1}{\varepsilon} = \frac{4\pi}{3}\left[\langle \mathbf{m}(\mathbf{r})\mathbf{M}(\mathbf{r})\rangle - \langle \mathbf{m}(\mathbf{r})\rangle \langle \mathbf{M}(\mathbf{r})\rangle\right] \tag{3.69}$$

Neglecting any boundary effects, eq. 3.69 is written as

$$\frac{\varepsilon-1}{\varepsilon} = \frac{4\pi V}{3}\left[\langle \mathbf{P}^2\rangle - \langle \mathbf{P}\rangle\langle \mathbf{P}\rangle\right], \tag{3.70}$$

3.4.2 Dielectric medium & surface term

Now, if we consider a computer simulation experiment describing a charged system per unit volume of periodic boundary replicas based on a spherical summation scheme and embedded in a dielectric continuum of ε' and applying an external electric field $\mathbf{E}_0$. We assume that the electrostatic energy per volume can be written as

$$u = u_0 - \mathbf{F}\mathbf{M} \tag{3.71}$$

where u_0 is given by eq. 3.6 is the Ewald contribution, $\mathbf{F}$ is the total field of the cavity which in our case is the simulation box and its replicas, and $\mathbf{M} = \sum_i q_i \mathbf{r}_i$ is the box's total dipole moment.

$$u = \underbrace{\sum_{1\leq i<j\leq N} q_i q_j \psi(\mathbf{r}_{ij}) + \frac{1}{2}\xi\sum_i^N q_i^2}_{Ewald} + \underbrace{\frac{2\pi}{3}\left\|\sum_{i=1}^N q_i\mathbf{r}_i\right\|^2}_{\text{spherical geometry + charge neutrality}} - \underbrace{\frac{1}{2}\frac{4\pi}{3}\frac{\varepsilon'-1}{\varepsilon'+\frac{1}{2}}\mathbf{M}^2}_{\text{dielectric medium}} - \underbrace{\frac{3\varepsilon'}{2\varepsilon'+1}\mathbf{E}_0\mathbf{M}}_{\text{external electric field}}, \tag{3.72}$$

In case where $\mathbf{E}_0 = 0$ after some calculations, eq. 3.72 is simplified to

$$u_{\mathbf{E}_0=0} = \underbrace{\sum_{1\leq i<j\leq N} q_i q_j \psi(\mathbf{r}_{ij}) + \frac{1}{2}\xi\sum_i^N q_i^2}_{Ewald} + \underbrace{\frac{2\pi}{(2\varepsilon'+1)}\left\|\sum_{i=1}^N q_i\mathbf{r}_i\right\|^2}_{\text{surface term}}, \tag{3.73}$$

which is also consistent with the surface term, which was introduced earlier in the case of spherical cells [39]. By choosing a dielectric medium $\varepsilon' \to \infty$, the eq. 3.73 is simplified to

$$u = \underbrace{\sum_{1\leq i<j\leq N} q_i q_j \psi(\mathbf{r}_{ij}) + \frac{1}{2}\xi\sum_i^N q_i^2}_{Ewald}. \tag{3.74}$$

Eq. 3.74 is the Ewald electrostatic energy. Indeed, under these conditions, molecular dynamics simulations followed by the electrostatic energy with conducting boundary conditions can be used to calculate the dielectric constant defined by eq. 3.70. Finally, we can conclude that the potential energy description is valid for describing a particle-charged-based system since the results are consistent with the dielectric theory.

3.4.3 External electric field

In molecular dynamics simulation, an external electric field can be applied as an external force

$$\mathbf{F}_{ext} = q_i\mathbf{E}. \tag{3.75}$$

This is how `GROMACS` [46] or `LAMMPS` [47] molecular dynamics machines work for systems under an external electric field. This interpretation is called *E-field ensemble* and the equations of motion are described by

$$-\nabla U_0 + q_i \mathbf{E} = m_i \frac{d^2 \mathbf{x}_i(t)}{dt^2}, \tag{3.76}$$

where U_0 is the system's potential with the electrostatic potential energy given by eq. 3.74 and $\mathbf{E}$ is the cavity field or, in our case, the simulation box field. Correspondingly, through eq. 3.76, the collection of the trajectories corresponds to the *E-field ensemble* of a system of enthalpy

$$\mathscr{F}(\mathbf{E}, v) = H_{PBC}(v) - \Omega \mathbf{PE}, \tag{3.77}$$

where $H_{PBC} = u_{\mathbf{E}_0=0}$ with v denoting a microstate and Ω the system's volume. The physical meaning of eq. 3.77 corresponds to close circuit boundary conditions with constant applied potential V (we constantly provide charges on the surface).

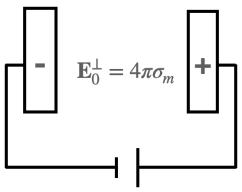

Figure 3.12 Charged plates. The schematic description of *E-field ensemble*. The ensemble is collected solving eq. 3.76

Closing this section, the simulation setup implemented in the present thesis is in alignment with the *E-field ensemble* 3.12. a valid framework to simulate an electrochemical system, experiencing an electric field in its vicinity.

Summary

The electrostatic treatment depends on the summation method of eq. 3.1 (toroidal or infinitely periodic) *geometry*, or the interaction truncation if the method of reaction field has been chosen (cubic or spherical). The properties of different systems are dependent on the *geometry* and the *electrostatic boundary conditions*. More details can be found elsewhere [41]. Finally, as we mentioned in the introduction, it is crucial to understand the electrostatic treatment in molecular dynamics simulations and try to simulate our system in a way that is as consistent as possible with the experimental settings in electrochemistry.

Part II

Chapter 4

The Effect of Electric Fields on the Structure of Water/Acetonitrile Mixtures

This chapter reproduces the publication "The effect of electric fields on the structure of water/acetonitrile mixtures", A. I. Sourpis, N. C. Forero-Martinez, F. Schmid, J. Electrochem. Soc. 170, 083508 (2023).
The research was carried out by myself. The text of the publication was drafted by myself and then finalized jointly by all authors.

4.1 Introduction

Liquid mixtures of water and acetonitrile are commonly used as solvent media in a variety of applications such as chromatography, organic synthesis, and electrochemistry. Liquid acetonitrile (CCN) is an aprotic amphiphilic molecule with a large dipole moment, which is a good solvent for many solutes, both polar and non-polar, and also mixes reasonably well with protic solvents such as water. For these reasons, CCN liquids and aqueous CCN solutions have been studied intensely for many decades [48] by experiments (e.g., NMR, spectroscopy, X-ray scattering) [49–57],theory [58–60], and simulations [61–63, 52, 64–67, 55, 68–74, 57], and a number of forcefields have been proposed that are specifically optimized for CCN [75–82].

Among others, these studies have revealed a tendency of CCN to form clusters or small domains in water (so-called microheterogeneities) [64, 68, 56] in the concentration regime of 20%-75% CCN [48, 56], and pronounced orientational correlations between neighboring CCN molecules [58, 59, 68, 70, 57]. The exact nature of correlation found in simulations somewhat depends on the force field: Earlier studies reported the formation of head-to-

head dimers [58, 59], whereas more recent studies suggested a preference for antiparallel orientations and head-tail orientations where two neighbor CCN are perpendicular to each other [68, 70, 57]. Also, the hydrogen bond distribution in water/CCN mixtures has been studied by various authors [51, 62, 52, 83]. Since CCN is aprotic, such studies give insight into the connectivity of water in water/CCN mixtures, which should have an impact on the proton transport in these fluids.

Studies of proton transfer phenomena in water mixtures are particularly interesting in hydrogen bonded systems. In particular, the effect of an external electric field on ethanol/water and methanol/water mixtures and their neat components has been studied via detailed ab-initio molecular dynamics simulations [84–88]. These results show changes in the ionic conductivity of mixed systems in comparison to neat systems, negligible changes in the H-bond structure [86], changes in probability distributions of α-helix H-bond characteristic lenghts [89] and an activation of chemical processes [90–92, 86] with increasing electric field.

In the case of water/CCN mixtures, with few exceptions [71, 74], the vast majority of studies have considered equilibrium liquids. In view of the wide use of CCN mixtures in electrochemistry, studies of the impact of electric fields on their structural properties are highly desirable. As a contribution to filling this gap, the present work presents a molecular dynamics study of the effect of externally imposed macroscopic electric fields on water/CCN mixtures. Since the choice of force field can have a critical influence on simulation results, we have first spent some effort into assessing and comparing different force fields. To this end, we have carried out simulations at zero electric field using different force fields for a range of concentrations, and compared the predicted thermodynamic and structural quantities to known experimental values and ab-initio results [68]. Based on this study, we have then selected one force field (Kowsari and Tohidifar, [80]) and focussed on experimentally relevant mixtures with a high CCN content (75 %) and studied them over a wide range of electric field strengths, ranging from the linear response regime to the strongly nonlinear regime. Our main findings can be summarized as follows: High electric fields significantly affect the relative orientation of neighboring CCN molecules. Interestingly, however, the structure of the hydrogen bond network is remarkably robust and hardly changes even in the nonlinear regime.

4.2 Methods

We performed classical atomistic molecular dynamics (MD) simulations of pure CCN and CCN-water mixtures in the bulk (periodic boundary conditions) with different CCN

concentrations (x_{CCN}) using the `GROMACS 2018.1` simulation package [46]. Unless stated otherwise, we use the rigid SPC force field [27] for water, the force field by Kowsari and Tohidifar [80] for CCN, and the Lorentz-Berthelot mixing rules to determine the mixed potential terms. Section 4.3 also shows results at $\mathbf{E} = 0$ for other CCN force fields [78, 77, 80, 79] and for the TIP4P water model [93] for comparison.

Here we use the term of macroscopic electric field, which is the cavity field $\mathbf{E}_c$ introduced in Chapter 3. The macroscopic electric field $\mathbf{E}$ points in the x direction. It contributes an extra force $q_i\mathbf{E}$ in the equations of motion of atoms i with charges q_i. We note that $\mathbf{E}$ is different from the so-called "applied field" $\mathbf{E}_0$, which is also sometimes used in the literature to characterize electric field effects. The relation between the macroscopic and the external electric field is given by eq. 3.67, where $\mathbf{E} = \mathbf{E}_c$ and $\mathbf{E}_0 = \mathbf{E}'$ accordingly. In a setting where the electric field $\mathbf{E}$ is assumed to be generated by a parallel plate capacitor, $\mathbf{E}_0$ denotes the electric field in a reference capacitor with same geometry and same surface charges, but which is empty inside instead of being filled with the (dielectric) CCN-water mixture. (In an empty reference capacitor with same geometry and same applied *voltage*, the electric field is still $\mathbf{E}$). In order to perform molecular dynamics simulations at constant $\mathbf{E}_0$, one must add a force term that couples to the polarization of the system [94–96]. In our system, however, we found such simulations to suffer from large finite-size effects, therefore we only show results for constant $\mathbf{E}$ here.

The number of CCN and water molecules depends on the CCN concentration and were chosen such that, at the pressure of 1 bar, simulation boxes roughly had the size $5 \times 5 \times 5$ nm^3 (see equilibration protocol below). For example, simulations at $x_{CCN} = 0.75$ correspond to 1216 CCN molecules and 406 water molecules, while 675 CCN molecules and 2028 water molecules were used in simulations at $x_{CCN} = 0.25$.

The time step used in the simulations was 1 fs. The LINear Constraint Solver (`LINCS`) algorithm [26] was used to constrain bonds involving hydrogen in the CCN molecule. This was done to improve the stability, since simulations with the Koverga potential [79] were found to sometimes crash if such constraints were not applied. The temperature was kept constant using the V-rescaling coupling method [12] with a relaxation time constant of 0.2 ps. Simulations at constant pressure (NPT) were done using the Parrinello-Rahman barostat with a time constant of 2.0 ps. Short range interactions such as the van-der-Waals interactions were cut off at 1.4 nm. The long-range electrostatic interactions were evaluated using the particle mesh Ewald (PME) method [97] with parameters 1.4 nm for the short-range part and grid spacing 0.12 nm for the Fourier part, using a fourth order interpolation scheme. The long-range forces and the Verlet lists used for neighbor searching were updated every 10 fs.

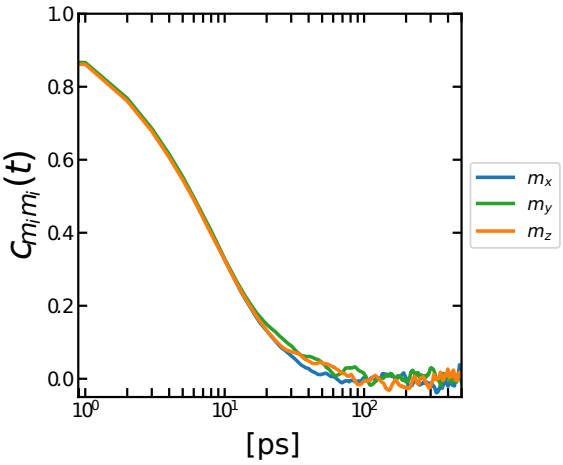

Figure 4.1 Autocorrelation function of CCN dipoles at zero electric field and CCN concentration $x_{CCN} = 0.75$. This simulation was done using the Kowsari force field [80] and SPC water.

All simulations were initialized by first filling a simulation box with the desired number of CCN molecules from a single CCN configuration taken from the Protein Data Bank [98] using the `PACKMOL` software [99]. Geometric overlapping was eliminated via an energy minimization step using the steepest descent algorithm. The CCN system was then solvated with water molecules using `GROMACS`, followed by another energy minimization step. The energy minimization steps were done at zero electric field. Then the electric field was turned on, if applicable, and the systems were equilibrated via a series of alternating simulations at constant volume (NVT ensemble) and constant pressure (NPT ensemble): (i) An initial equilibration over 10 ns in the NVT ensemble at $T = 298$ K; (ii) An NPT simulation over 25-35 ns at the pressure of 1.0 atm, in order to adjust the size of the simulation box; (iii) A final equilibration in the NVT ensemble over 25 ns. Production runs had a total length of 100 ns. In the force field comparison simulations described in Section III, the initial equilibration (i) included an NVT simulation of 10 ns at temperature $T = 400$ K followed by an annealing procedure from $T = 400$ K to $T = 298$ K over 10 ns.

After equilibration, NVT simulations over 100 ns were carried out for data collection and analysis (5-10 ns in the force field comparison). To assess the characteristic time scales of our system, we have computed the dipole time autocorrelation function for CCN molecules, see Figure 4.1. It is found to decay to zero within 100 ps. The total simulation time in the production runs thus corresponds to more than 10^4 rotational relaxation times of CCN. In these, we used the last 15 ns for determining radial distribution functions, the last 25 ns for

determining combined distribution functions (see below), and the full 100 ns for carrying out the analysis of hydrogen bond networks.

Specifically, the radial distribution function of particles A and B is defined by

$$g_{AB}(r) = \frac{\rho_B(r)}{\langle \rho_B \rangle} = \frac{1}{\langle \rho_B \rangle} \frac{1}{N_A} \sum_{i \in A}^{N_A} \sum_{j \in B}^{N_B} \frac{\delta(r_{ij} - r)}{4\pi r^2}, \tag{4.1}$$

where $\rho_B(r)$ is the particle density of type B at a distance r around particle A. The normalization factor $\langle \rho_B \rangle$ is determined from the particle density of type B particles, averaged over all spheres around particles A with radius $r_{max} = L/2$ where L is the simulation box length.

As another quantity to characterize the local structure of our fluids, we calculate the combined distribution function (CDF) of angular and radial correlations of CCN molecules. We analyze the last 25 ns of the production runs to obtain the CDF using the `Travis` trajectory analyzer [100]. The CDF is defined as:

$$g_{CDF}(r, \theta) = \frac{1}{N} \sum_{i}^{N} \sum_{j}^{N} \langle \delta \left(r - r_{ij} \right) \delta \left(\theta - \theta_{ij} \right) \rangle, \tag{4.2}$$

where r_{ij} is the distance between the center of masses of the ith and jth CCN molecules and the mutual orientation is defined by θ_{ij}, the angle between CCN “molecular" vectors. These vectors are defined for each CCN molecule as the vector connecting the carbon atom of the CH_3 group with the nitrogen atom.

4.3 Comparison of force fields

As mentioned in the introduction, several CCN force fields have been proposed in the literature [75–80], both united-atom models [76] and all-atom models with explicit hydrogen [75, 77–80]. In preparation of our study, we have thus compared the four more recently proposed force fields [77–80] by carrying out simulations of systems with different CCN concentrations at zero electric field and comparing the structural and thermodynamic properties to experimental data and available ab-initio simulations [68]. In addition, we have also compared results obtained with two different established water models, namely the three-site rigid SPC model [27] and the four-site TIP4P model [93].

All CCN models considered in this work are all-atom models and use the AMBER functional form [101]. The intramolecular interactions include harmonic bonding and

bending contributions, but no torsional potential, and the non-bonded potentials include Lennard-Jones and Coulomb potentials. The force fields by Grabuleda et al. [77] and Nikitin and Lyubartsev [78] are based on the AMBER model parameters, and were tuned to either fit structural properties and density of pure CCN or reproduce experimental CCN-water mixture densities, the heat of evaporation and dielectric properties. Koverga et al. [79] developed an entirely new set of parameters to focus on the structural, dynamic, and thermodynamic properties of pure CCN. Most recently, Kowsari et al. [80] recalibrated the AMBER-based models to reach an agreement with dynamical properties such as the self-diffusion coefficient and thermodynamic properties of pure CCN while providing an appropriate qualitative description of the liquid CCN structure.

4.3.1 Density

We begin with comparing the density of the mixtures at different CCN mole fractions x_{CCN} as obtained with the different force fields. The results are given in Table 4.1. The best agreement with experiments is obtained with the Nikitin and the Kowsari force fields. Specifically, the results for the Kowsari force field combined with TIP4P water are in excellent agreement with the experimentally reported density values for all liquid-water mixtures except pure CCN. When combined with the SPC water model, the agreement between simulations and experiment is still very good.

Table 4.1 Density (kg/m^3) at pressure 1 bar obtained from simulations with different CCN and water force fields as indicated and compared to experiments.

x_{CCN}/ρ	0.10	0.50	0.90	neat CCN
Kowsari [80]/SPC[27]	939.7 ± 0.03	840.6 ± 0.1	795.6 ± 0.1	788.6 ± 0.3
Kowsari [80]/TIP4P[93]	957.8 ± 0.1	845.6 ± 0.1	793.8 ± 0.1	788.6 ± 0.1
Koverga [79]/SPC[27]	938.3 ± 0.06	834.3 ± 0.1	779.6 ± 0.2	770.7 ± 0.2
Koverga [79]/TIP4P[93]	956.8 ± 0.03	842.0 ± 0.2	781.0 ± 0.1	770.7 ± 0.2
Nikitin [78]/SPC[27]	933.3 ± 0.04	846.0 ± 0.1	789.3 ± 0.1	773 ± 5[78]
Grabuleda [77]/SPC[27]	922.2 ± 0.09	796.0 ± 0.07	742.2 ± 0.06	735.3 ± 5[77]
Experiment [49]	958.6	845.1	786.3	776.7

4.3.2 Radial distribution functions

Next we consider the radial distribution functions (RDFs) (see Eq. 4.1), which allow us to understand how CCN and water molecules are, on average, radially packed with respect to each other.

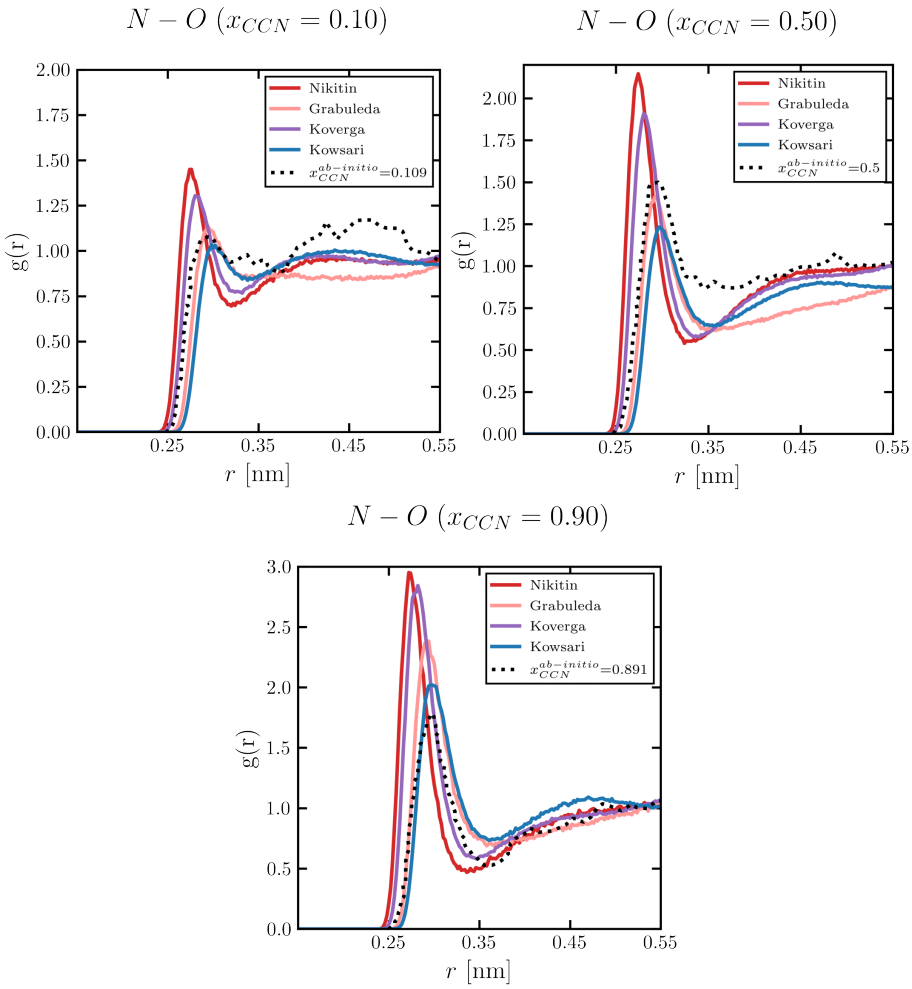

Figure 4.2 Radial distribution function of nitrogen *N* of acetonitrile and the oxygen *O* of water for different mole fraction as indicated for each plot, where force fields Nikitin [78], Grabuleda [77], Kalugin [79], Kowsari [80] are compared to ab-initio results [68].

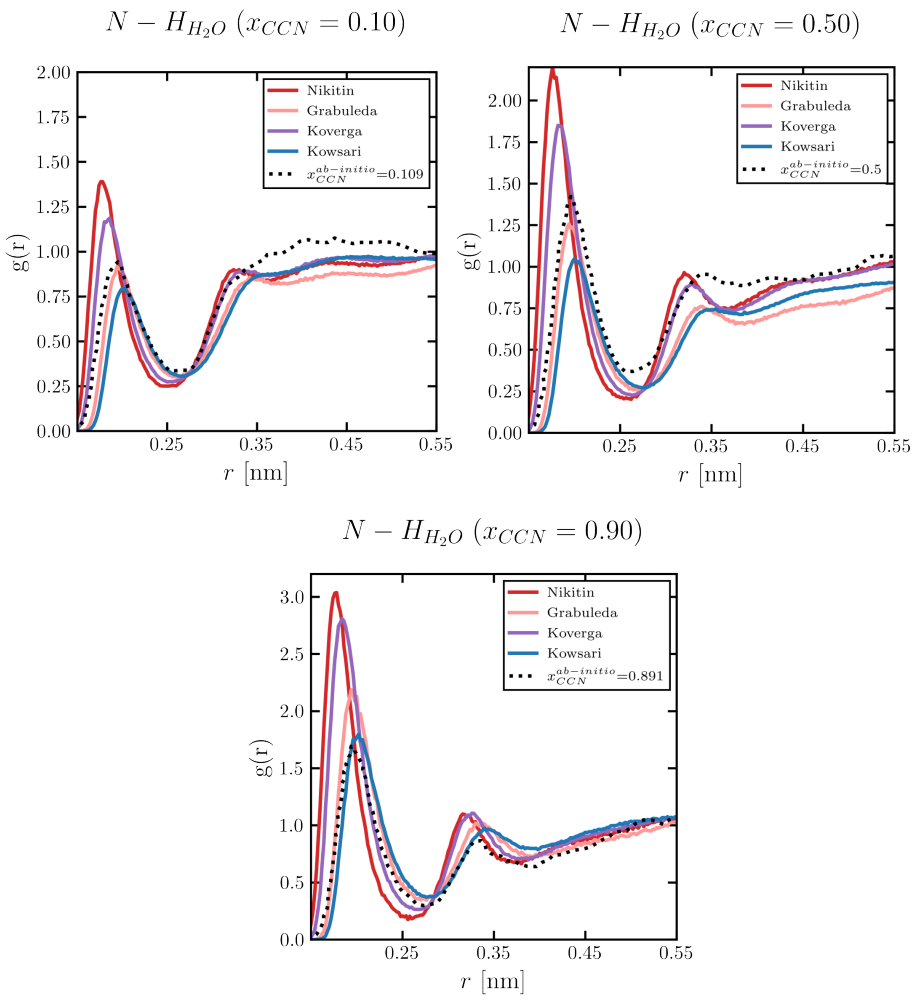

Figure 4.3 Same as Figure 4.2 for nitrogen atoms in *CCN* and hydrogen atoms in water.

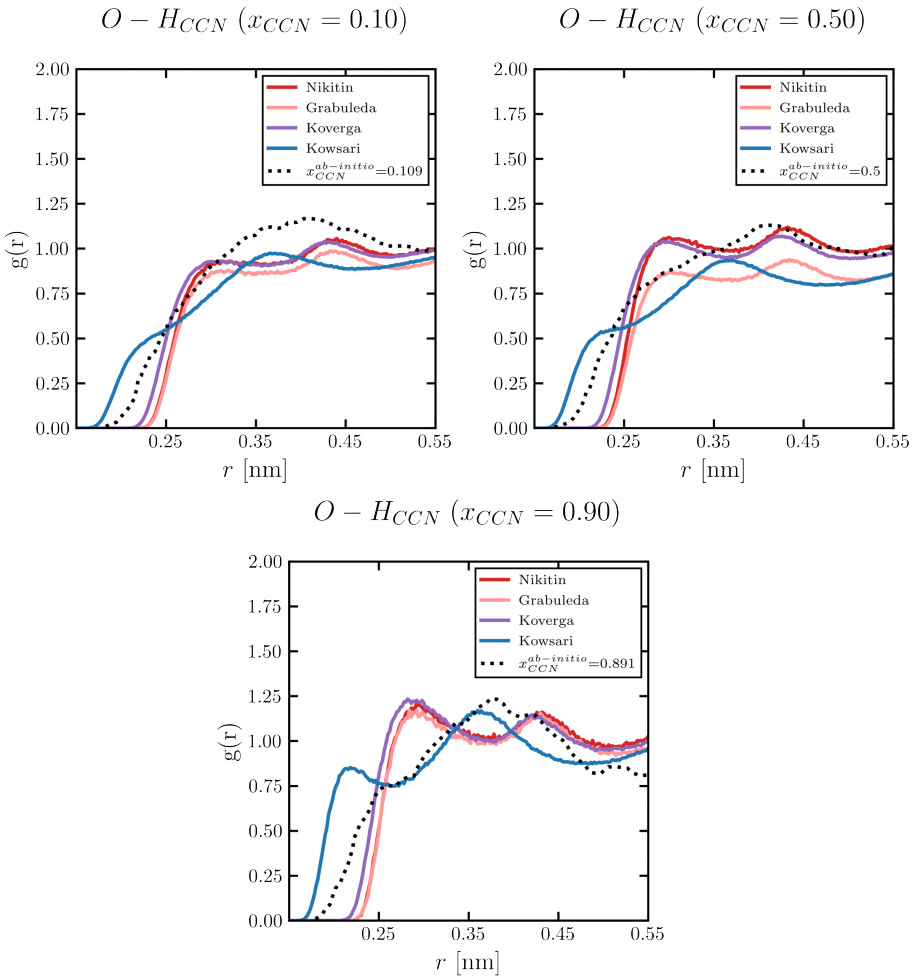

Figure 4.4 Same as Figure 4.2 for oxygen atoms in water and hydrogen atoms in *CCN*.

Figures 4.2, 4.3 and 4.4 show selected RDFs for atom pairs between CCN and water molecules, comparing ab-inition simulations of Chen and Sit [68] and our results obtained with the classical force fields [77–80] and SPC water. (Additional data for RDFs can be found in the Appendix A). These data can be used to evaluate our classical force fields.

In the case of the correlation function involving nitrogen (Figures 4.2 and 4.3), all force fields roughly capture the basic structure of the RDFs and the positions of the peaks and minima. The height of the first peak is generally too high in the simulations with the Nikitin and Koverga force fields [78, 79] and lowest in the simulations with the Kowsari force field [80]. At high CCN concentrations, the RDFs obtained with the Kowsari force field are in very good agreement with the ab-initio reference data. In the case of the correlation functions H-O_W between CCN hydrogen and water oxygen, the comparison of classical force field simulations with the ab-initio reference simulation is less favorable: The RDFs obtained from classical simulations are much more structured than the reference ones from the ab-initio simulations. In particular, they exhibit a peak at distance $r = 0.25$ nm for all CCN concentrations which is absent in the ab-initio simulations. However, this peak is less pronounced in the simulations with the Kowsari force field [80] than in the other simulations.

We conclude that the Kowsari force field [80] captures the local structure of CCN/water mixtures better than the other force fields and therefore choose to use this force field for the subsequent studies that will be described in the next section. For reasons of computational efficiency, we combine this with the SPC water model, which it is computationally much less expensive than the TIP4P water model and produces less noisy data in runs of similar length.

4.4 Impact of electric fields on CCN-Water mixtures

We turn to discussing the effect of macroscopic electric fields on the properties of CCN/water mixtures. Here, we focus on systems with the CCN mole fraction $x_{CCN} = 0.75$, i.e., high CCN content, a composition which is interesting for use in electrolysis cells. As discussed in the previous section, we use the Kowsari CCN force field [80] in combination with the SPC water model. For the convenience of the reader, the force field parameters of the CCN force field are summarized in Table S1 in Appendix A.

4.4.1 Polarization

As our system contains no free charges, but molecules with a large dipole moment $\mathbf{m}_i$, the most obvious effect of a macroscopic field $\mathbf{E}$ is to orient the dipoles. We define the total dipole moment as $\mathbf{M} = \sum_i \mathbf{m}_i$ and also consider separately the contributions $\mathbf{M}_{CCN}$ and $\mathbf{M}_{H_2O}$

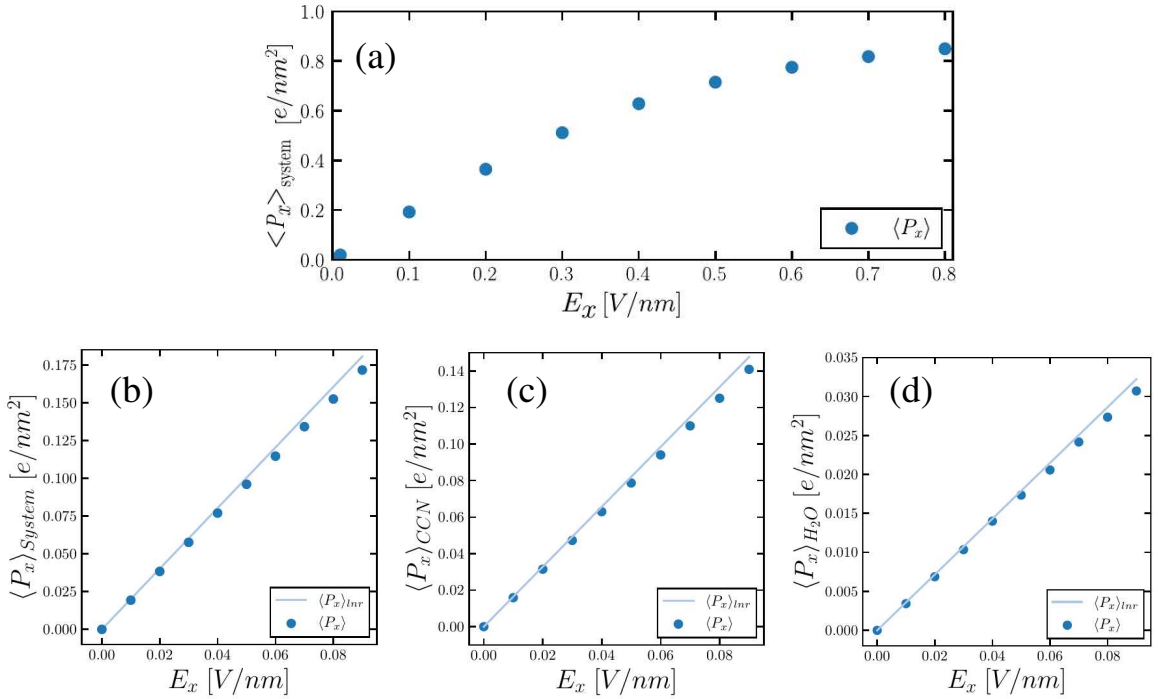

Figure 4.5 Total polarization (a,b) and corresponding CCN (c) and water contributions (d) as a function of the macroscopic field. The solid lines show the linear response value obtained from Eq. (4.4).

of acetonitrile and water. The polarization of the system (in the absence of free charges) is then given by $\mathbf{P} = \mathbf{M}/\Omega$, where Ω is the volume of the system.

Since the system contains no free charges, just well-defined dipoles, the additional electrostatic energy associated with a spatially homogeneous electric field $\mathbf{E}$ can simply be written as [102] $\Delta H_{\mathbf{E}} = -\sum_i \mathbf{E} \cdot \mathbf{m}_i = -\mathbf{E} \cdot \mathbf{M}$,

and the total energy of a given configuration $\mathscr{C}$ is given by

$$H(\mathscr{C}) = H_0(\mathscr{C}) - \mathbf{E} \cdot \mathbf{M}. \tag{4.3}$$

Here $H_0(\mathscr{C})$ refers to the energy of the same configuration $\mathscr{C}$ in the absence of a macroscopic field. This expression (4.3) also remains valid if the amplitudes $|\mathbf{m}_i|$ of molecular dipoles are affected by the electric field and even if the molecular dipoles are induced by the field. We note that the situation is more complicated if a system contains free charges such as ions. In this case the correct expression for the polarization $\mathbf{P}$ is less obvious and the treatment of periodic boundary conditions requires extra care [31, 103].

For small macroscopic electric fields, the energy contribution (4.3) can be treated as a perturbation and linear response theory can be applied. In the linear regime, one thus expects

the thermal average of the polarization to be given by

$$\langle \mathbf{P} \rangle_{linear} = \frac{\beta \mathbf{E}}{\Omega} \langle \mathbf{MM} \rangle_{\mathbf{E}=0} \tag{4.4}$$

where $\beta = 1/k_B T$ is the Boltzmann factor and **MM** refers to the tensor product $M_i M_j$. The corresponding equation also holds for the individual contributions of water and CCN to the total polarization if **M** is replaced by $\mathbf{M}_{H_2O}$ and $\mathbf{M}_{CCN}$, respectively.

Figure 4.5 shows the simulation results for the polarization (symbols) and compares them with the linear response prediction, Eq. (4.4). From these curves, one can infer that the linear regime extends up to roughly $|\mathbf{E}| \sim 0.1\,V/\text{nm}$. In the nonlinear regime, the curves for the polarization versus macroscopic field flattens. The crossover from linear to nonlinear becomes even clearer if one inspects the susceptibility $\chi(E)$, defined *via* $\mathbf{P} = \varepsilon_0 \chi(E)\mathbf{E}$ as the ratio of the polarization and the macroscopic field, which is shown in Figure 4.6 a) as a function of E. It is initially constant ($\chi \approx 35$) and then decays with quasi constant slope ($\chi(E) \approx 38 - 24\,E\text{nm}/V$) for field amplitudes higher than $E \sim 0.15 V/\text{nm}$. Comparing the corresponding dielectric constant in the linear regime $\varepsilon_r = 1 + \chi \approx 36$, with the experimental value [104] for CCN/water mixtures at 75% CCN and temperature 25°, $\varepsilon_{r,\text{exp}} \approx 45$, one finds that it is of similar order, albeit a bit too low. The difference can partly be attributed to the fact that the simulations can only capture the reorientation contribution to ε, since we use a non-polarizable force field. In the nonlinear regime, the dielectric constant, defined *via* $\mathbf{D} = \varepsilon_r \varepsilon_0 \mathbf{E}$, is still isotropic and decreases with E following $\varepsilon_r(E) = 1 + \chi(E)$ (see also Eq. (22) in Ref. [95]). However, the electrostatic interactions between free charges in the system are governed by an effective dielectric tensor which is anisotropic (see SI for the derivation). Its components are given by $\varepsilon^{\perp}_{r,\text{eff}} = \varepsilon_r$ perpendicular to the macroscopic field, and $\varepsilon^{||}_{r,\text{eff}} = 1 + \chi^d(E)$ parallel to the field, where χ^d is the differential susceptibility, $\chi^d(E) = \frac{1}{\varepsilon_0} \mathrm{d}P/\mathrm{d}E$. Figure 4.6b) shows ε_r along with $\varepsilon^{||}_{r,\text{eff}}$ and $\varepsilon^{\perp}_{r,\text{eff}}$. We note that $\varepsilon^{||}_{r,\text{eff}}$ almost decays to one at high macroscopic fields E_x. This is consistent with the results of Daniels et al. for pure CCN[71], who exploited the fluctuation relation $\chi^d \propto \langle \mathbf{P^2} \rangle_{\mathbf{E}} - \langle \mathbf{P} \rangle^2_{\mathbf{E}}$ and calculated $\varepsilon^{||}_{r,\text{eff}}$ directly from the polarization fluctuations.

We should note that the highest fields in Figure 4.5 (a) most likely exceed the dielectric strength of the mixture, i.e., the field amplitude where dielectric breakdown sets in. The dielectric strength of pure water is around $|\mathbf{E}|_{db} \sim 0.07\,V/\text{nm}$ in the bulk and can reach values of $|\mathbf{E}|_{db} \sim 0.4\,V/\text{nm}$ or more in narrow gaps [105].

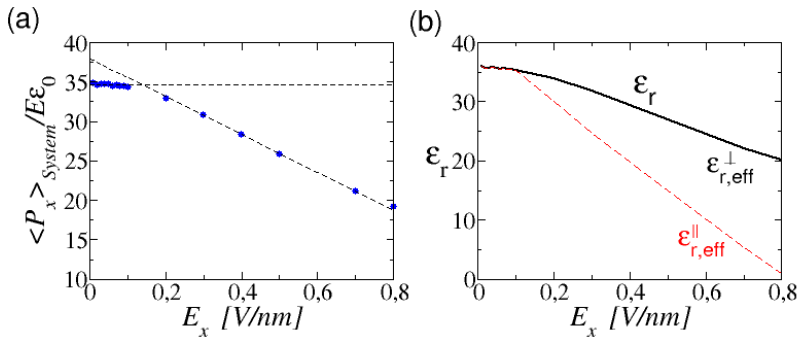

Figure 4.6 (a) Ratio $\langle P_x \rangle_{\text{System}}/(E\varepsilon_0)$ as a function of the macroscopic field. The dashed lines illustrate the crossover from a constant behavior to a linear decay. (b) Resulting dielectric constant and effective dielectric constant

4.4.2 Local structure and correlations

Having identified the linear response regime, we now search for signatures of nonlinear behavior in the local correlations of the CCN/water mixture. Figure 4.7 shows radial distribution functions $g(r)$ for selected atom pairs, namely, nitrogen/hydrogen water and nitrogen/nitrogen, over a wide range of applied electric fields **E**. The influence of the electric field on $g(r)$ turns out to be almost negligible as also observed in methanol/water mixtures [86]. The different curves are almost identical in the case of atom pairs between CCN and water, and still very close to each other in the case of atom pairs between two CCN molecules. The pair distribution functions of other atom pairs, shown in Appendix A, confirm this picture.

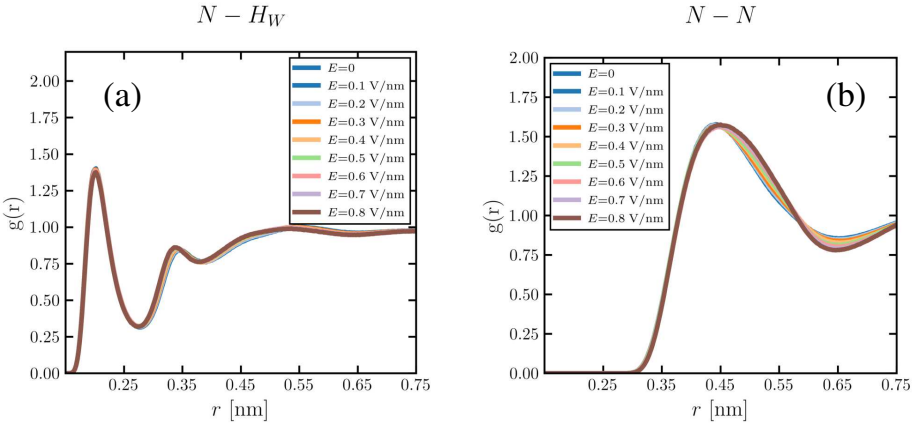

Figure 4.7 Radial distribution functions at $x_{CCN} = 0.75$ for different electric fields as indicated between (a) nitrogen and water hydrogen, and (b) two nitrogens

This however changes when we inspect the orientational correlations of CCN molecules. As discussed in the introduction, experimental as well as computational studies suggest that neighboring CCN molecules have a tendency to adopt an antiparallel orientation, regardless of whether they are in a pure or solvated state [68, 69, 79, 70, 73, 57].

We use the combined distribution function (CDF) of angular and radial correlations to gain insight into the mutual orientation of the CCN molecules and how the distance between their center of masses affects these orientations, see Equation (4.2) in subsection 4.3.2. The CDF allows us to understand how the molecules arrange not only in a radial manner but also how they orient relative to each other. We evaluate this function up to a distance of 0.6 nm, corresponding to the onset of the first minimum in the radial distribution function of the center of masses of CCN (Figure A.12 in Appendix A). Figure 4.8 shows our results for zero applied field, $\mathbf{E} = 0$. The CDF, $g_{CDF}(r, \theta)$, has a maximum at $\theta = 180^\circ$ and $r \sim 0.37$ nm, corresponding to configurations where the closest neighbors are at a distance of around 0.37 nm and the mutual orientation of CCN molecules is antiparallel. Earlier studies of pure CCN liquids [70, 57] have reported a second peak suggesting an additional preference for perpendicular orientations with head-tail orientation. This peak is absent in our simulations of CCN/water mixtures.

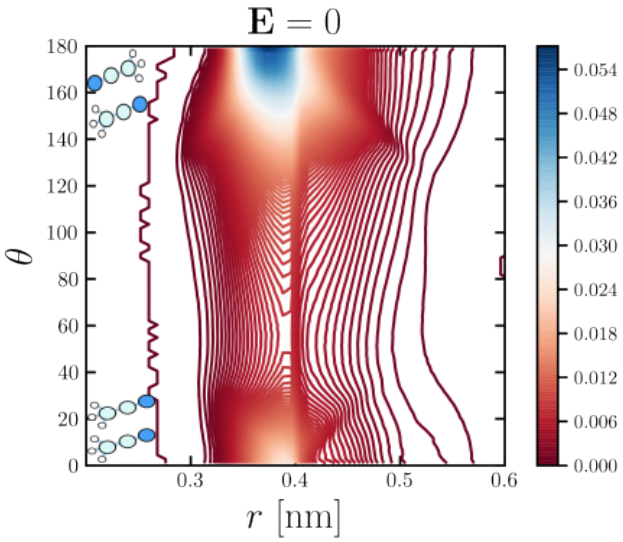

Figure 4.8 Combined distribution functions (CDFs) between the center of mass of CCN first neighbors and the θ angle between vectors defined along the CCN molecules in CNN/water mixtures at $\mathbf{E} = 0$.

In the presence of high macroscopic electric fields, the orientation correlation between neighboring CCN molecules changes qualitatively. This is demonstrated in Figure 4.9, which shows countour plots of the CDF between first neighbor molecules (same as Figure 4.8)

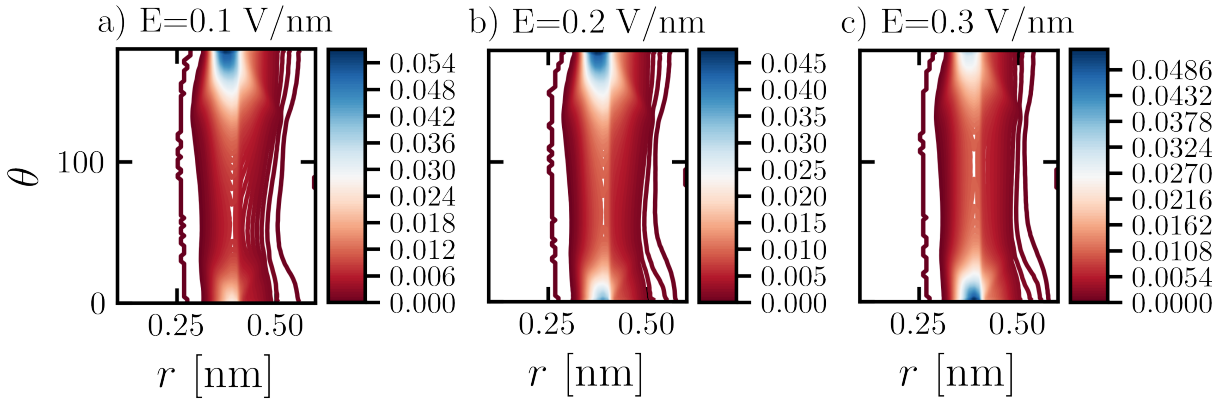

Figure 4.9 Same as Figure 4.8 for different macroscopic fields E as indicated.

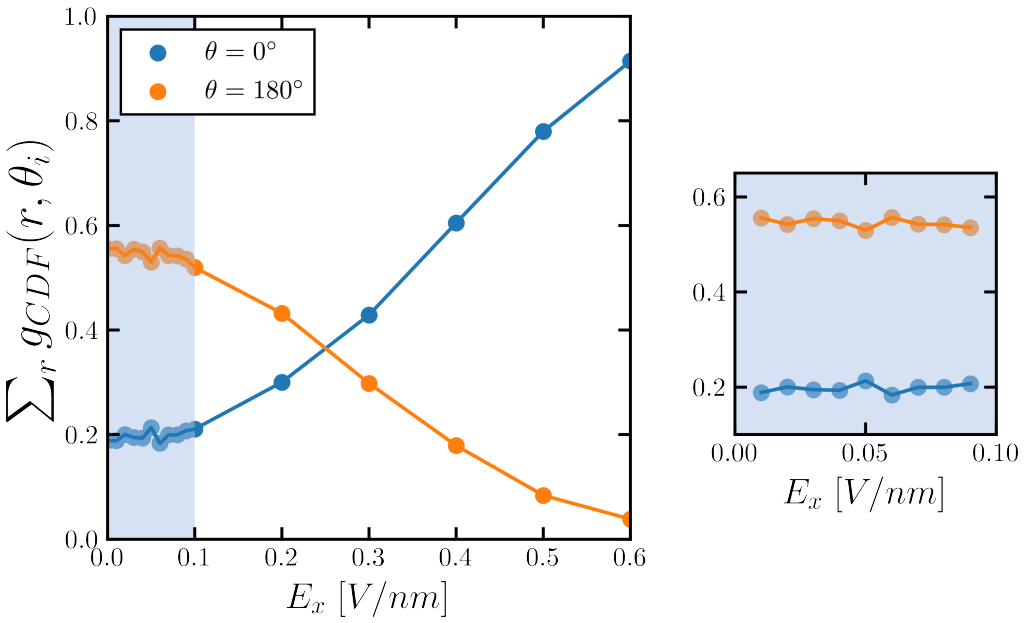

Figure 4.10 Radially integrated combined distribution function from Fig. 4.9 at the two angles $\theta = 0°$ and $\theta = 180°$ as a function of macroscopic field E_x. The right panel shows a blowup at small macroscopic fields E_x.

for three different applied fields, $|\mathbf{E}| = 0.1$V/nm, 0.2V/nm, and 0.3V/nm. With increasing macroscopic field, the peak corresponding to the antiparallel orientation gradually disappears, and instead, a peak at $\theta = 0°$ (parallel orientation) emerges. The change in orientation explains the slight changes in the radial distribution function $g(r)$ of atom pairs between two CCN molecules as a function of the electric field in Figure 4.7 b) and Figure A.9 in Appendix A.

In order to assess whether this is a nonlinear effect, we have computed the integrated angular correlation function, which we define as the radial integral $\int_0^{r_{\text{cut}}} \mathrm{d}r\, g_{CDF}(r,\theta)$, where the upper limit, $r_{\text{cut}} = 0.6$ nm corresponds to the first minimum of the center-of-mass correlation of CCN molecules as discussed above. The result is shown in Figure 4.10. The curves clearly show the gradual transition between a state where neighboring CCN molecules mostly show an antiparallel orientation to a state where they are mostly parallel to each other. They also demonstrate that this is clearly a nonlinear effect: Initially, for small fields, the integrated angular correlation functions are roughly independent of the applied field. Around $E \sim 0.1\,V/\text{nm}$, they start to change such that the integrated CDF at $\theta = 0°$ (parallel orientation) grows at the expense of the integrated CDF at $\theta = 180°$ (antiparallel orientation).

4.4.3 Hydrogen bond network and micro-heterogeneities

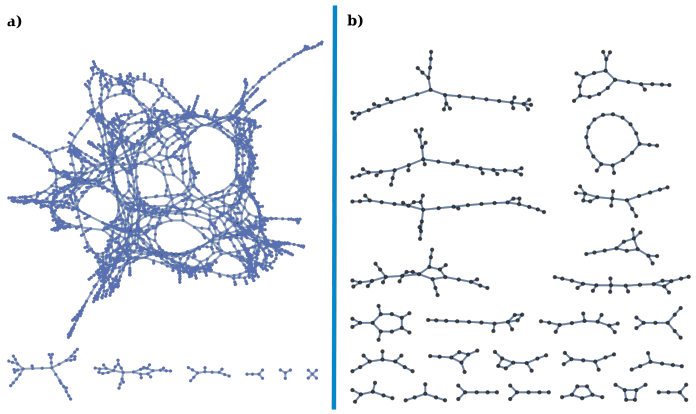

Figure 4.11 Examples of planar representations of hydrogen bond networks via graphs. Each node corresponds to a molecule of water or acetonitrile. For every mole fraction, the hydrogen bond network forms clusters. Panel (a) shows an example for a configuration at $x_{CCN} = 0.25$ containing one large and highly interconnected cluster and several rather small clusters. Panel (b) shows an example for a configuration at $x_{CCN} = 0.75$ showing many smaller elongated and often tree-like clusters.

Finally, we study the structure of the hydrogen bond network in our mixtures, which can give indirect information on potential channels for proton transport in the system. Since classical molecular dynamic simulations do not explicitly account for proton delocalization, the first problem consists in identifying hydrogen bonds or potential hydrogen bonds in classical configurations. Different hydrogen bond definitions have been proposed in the literature [106, 107]. In the present study, we use the `CHIMERA` [108] software to identify the hydrogen bond network. The `CHIMERA` tool applies a geometric criterion to compute a three dimensional hydrogen bond distribution, and therefore a probability of hydrogen-

bond formation, for each hydrogen-bonding site [109]. Some more details can be found in Appendix A. Once we have identified hydrogen bonds, we can identify clusters and represent hydrogen bond networks via graphs, where the nodes correspond to hydrogen donor and/or acceptor molecules and the edges to hydrogen bonds. We note that in rare cases, the CHIMERA software may assign two hydrogen bonds to the same CCN molecule, see Figure 4.11 c). Even though such complexes do exist [110], the CHIMERA assignment in such cases is most likely wrong. Nevertheless, the analysis provides a useful tool to evaluate the geometric network of the molecules in the system.

Figure 4.11 shows representative examples of two-dimensional graph descriptions of the hydrogen bond network for CCN-water mixtures at CCN concentrations of (a) $x_{CCN} = 0.25$ and (b) $x_{CCN} = 0.75$. Every node represents a molecule, either CCN or water, and every connecting line corresponds to a hydrogen bond. In addition, these clusters might contain cycles of hydrogen-bonded chains. For low CCN concentrations, a single large graph dominates containing many interconnected cycles, whereas tree graphs are abundant at high CCN concentrations. Dangling ends, in this case, mostly correspond to CCN molecules where further hydrogen bonding is impossible. These observations are similar to those reported in Ref. [83] for water/methanol mixtures.

To describe microheterogeneities in these binary mixtures, it is useful to identify sub-classes of hydrogen-bonded clusters inside the simulation box [10]. The first sub-class represents the largest cluster, the other sub-classes represent the smaller ones. Figure 4.12 shows one example of a large cluster in a configuration taken from a trajectory of 100 ns at CCN mole fraction $x_{CCN} = 0.75$ in graph representation (a) and in real space (b). One can clearly see that the water molecules in the hydrogen-bonded cluster are mainly inside, and partially surrounded by CCN molecules. Panel (c) in the same Figure specifically highlights molecules that belong to cycles in hydrogen-bond network. We note that in rare cases, the Chimera may wrongly assign two hydrogen bonds to the same CCN molecule. This can be seen in one of the cycles (light red) which contains, shown as largest bead, a CCN molecule.

To quantify the properties of the hydrogen bond network and the impact of macroscopic electric field, we have calculated histograms of the number of molecules $N_{molecules}$ in the largest hydrogen bond cluster of the configurations at $x_{CCN} = 0.75$. The results are shown in Figure 4.13. The curves exhibit a pronounced maximum around $N_{molecules} \sim 60$, followed by a long tail which decays to zero at $N_{molecules} \sim 200 - 250$. The total number of water molecules in these configurations is around 2000, hence even the largest cluster contains only a small fraction. Apart from a very small shift to larger $N_{molecules}$, the shape of the curves is almost unaffected by macroscopic fields.

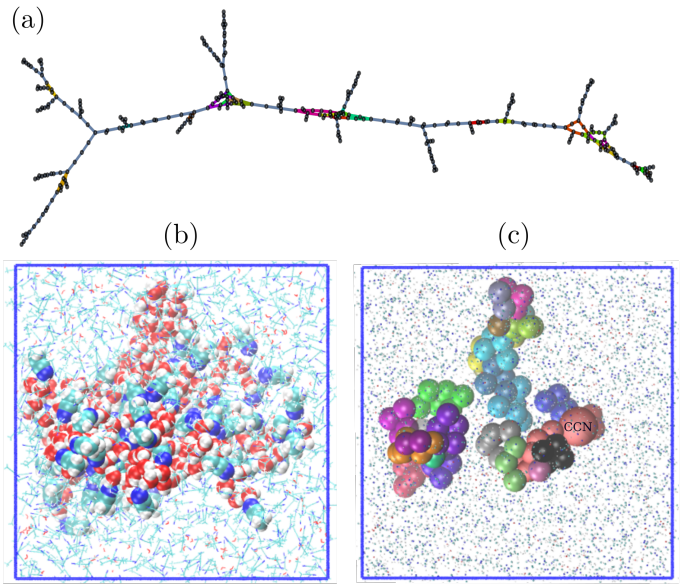

Figure 4.12 Example of a large hydrogen-bonded cluster in a CCN-water mixture at x_{CCN}=0.75, as determined by the Chimera tool[108]. (a) Graph representation. Dangling ends correspond to CCN molecules. Different cycles in the graph are marked by different colors. (b) Real space all-atom representation of the molecules belonging to this network. Oxygen atoms in water are red, nitrogen atoms in CCN are blue. (c) Real space coarse-grained representation of cycles inside the same graph. Every bead corresponds to a molecule. Different colors correspond to different cycles, the color coding is the same as in (a). The largest bead represents a CCN molecule, which is part of a cycle because two hydrogen bonds were assigned to it (most likely wrongly, see text).

Furthermore, we have also analyzed the cycles (see Figure 4.12 (c)) in the largest clusters of our configurations and evaluated histograms of the number of molecules that constitute a cycle. The results are shown in Figure 4.14. Our results for electric field zero ($\mathbf{E} = 0$) are consistent with an earlier study of Bergman and Laaksonen [62], who determined histograms for the lengths of all cycles in the hydrogen bond network of water/CCN mixtures. The shape of the histograms is very similar, and Bergman and Laaksonen also report a maximum at cycle length five. Here, we find that applying an macroscopic field has no impact at all on the distribution and number of cycles in the largest cluster.

4.5 Conclusions

In the present work, we have studied the impact of macroscopic electric fields on the structure of water/acetonitrile mixtures. We find that these systems exhibit a nearly linear response to

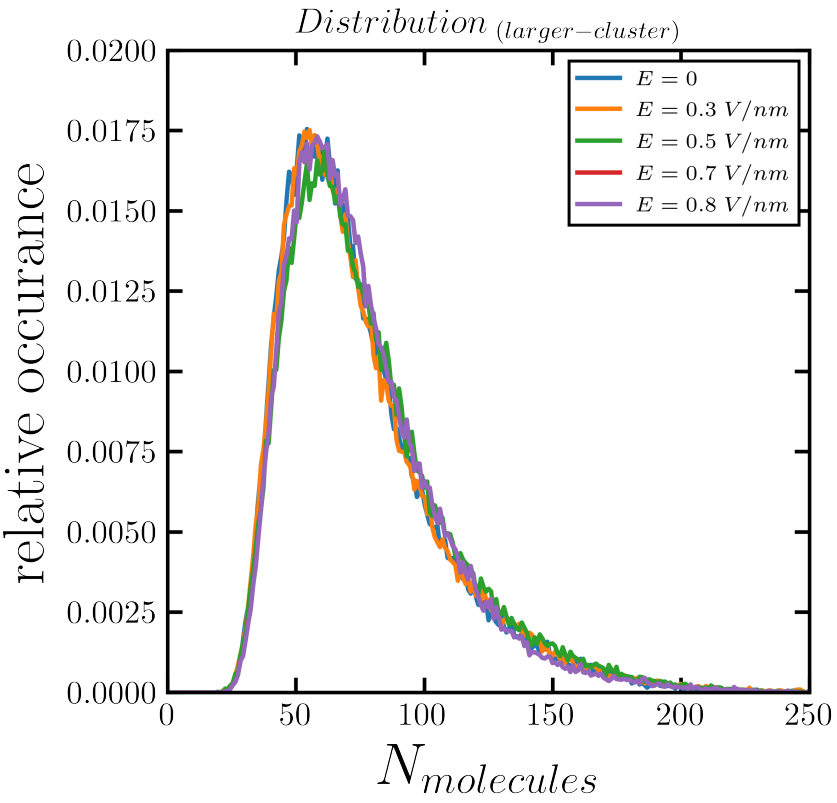

Figure 4.13 Distribution of the number of molecules $N_{molecules}$ in the largest hydrogen bond cluster of configurations at $x_{CCN} = 0.75$ for different applied electric fields as indicated.

electric fields up to field amplitudes of around $E \sim 0.1\,V/\text{nm}$. The most prominent signature of nonlinear behavior is a reorientation of neighboring CCN molecules from antiparallel, which is predominant at field zero, to parallel, which dominates at very high fields. However, the characteristics of the hydrogen bond network seem largely unaffected by this up to electric field strengths which are high above the dielectric breakdown limit in real systems. In this context, we have also investigated the signatures of microheterogeneities in the hydrogen bond network of the water/acetonitrile mixtures at high acetonitrile content. We found that the connected hydrogen bond clusters in the mixtures correspond to compact clusters in real space which are partially surrounded by acetonitrile molecules, which correspond to dangling ends in the graph representation of the cluster. This supports the view that acetonitrile acts as a confinement matrix for water clusters. The present study was partly motivated by a recent intriguing observation in narrow-gap electrolysis cells [11], where it was found that such mixed solvents may support currents even in the absence of supporting electrolyte if the gaps are very small, i.e., the applied fields are high. In these experimental settings, the gap width is of the order of millimetres and the fields thus never exceed 1 V/μm, which is deep in

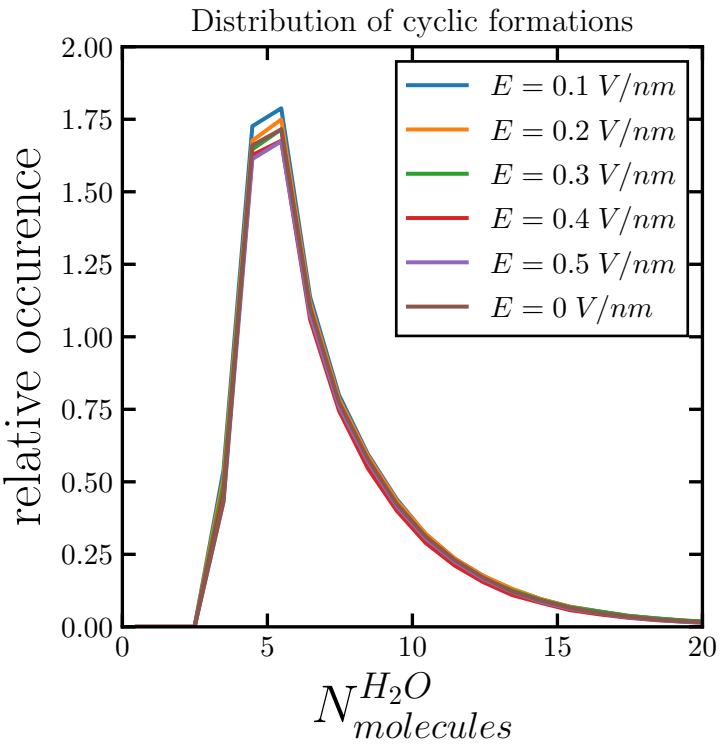

Figure 4.14 Histogram of the number of molecules belonging to a cycle formation within the largest cluster of a configuration for different macroscopic electric fields as indicated. Cycles with 5 molecules dominate.

the linear response regime according to the present study. Our study does not provide any evidence of significant structural changes in this regime. Therefore, we must conclude that we cannot explain the experimental results. Further studies will be necessary which possibly will have to include the effect of electrodes and impurities.

Part III

Chapter 5

Conclusions

We have used molecular dynamics simulations as a computational tool to study an electrochemical system.

Part I: The first part introduces molecular dynamics simulations implemented on GROMACS framework. The equations of motion were integrated using classical force fields associated with the system's dynamical description. Next, the statistical mechanics interpretation demonstrates how the thermodynamic properties can be derived in the presence of an external perturbation in the linear response theory. The first part ends by showing that the dielectric theory is consistent with the electrostatic treatment of bulk systems in molecular dynamics simulations.

Part II: The aim of this part is to apply molecular dynamics simulations to study the effect of the electric field in a solution of water and acetonitrile mixtures. Initially, the correct Force field parameters were chosen by comparing different AMBER-based force fields (see Chapter 2) as a benchmark. However, we were focused on the most microheterogeneous state, which corresponds to $x_{CCN} = 0.75$ closely related to the experimental setup [11]. Then the phenomena of the external electric field were analyzed, based on the linear response regime (see Chapter 2) in a consistent manner with the dielectric theory (see Chapter 3). Indeed, this was achieved by using an external electric field $\mathbf{E} = E_0\hat{x}$. Our main hypothesis to explain the conductivity for the case of water acetonitrile mixtures was based on the hydrogen bond network physiology. The key findings of the current analysis are that the hydrogen bond network properties such as the biggest cluster size distribution and the cyclic formation distribution remain unchanged even for the electric field in the non-linear response regime. However, very interesting phenomena occur as the electric field is increased and reaches the non-linear regime, such as the orientational flipping of the neighboring acetonitrile molecules from the parallel to the anti-parallel orientation. Last but not least, studying the system of water and acetonitrile interfaces seems a very interesting system. Finally,

physical electrochemistry using molecular dynamics simulations is a promising field for analyzing dynamical processes for electrochemical systems that cannot be detected easily using experimental techniques i.e. the hydrogen bond network analysis or the orientational formation of the neighboring molecules. Furthermore, techniques such as machine learning or transition path sampling can be used to explore the solid-liquid interface and elucidate its dynamics.

Bibliography

[1] Sung Sakong, Jun Huang, Michael Eikerling, and Axel Groß. The structure of the electric double layer: Atomistic versus continuum approaches. *Current Opinion in Electrochemistry*, 33:100953, 2022.

[2] Céline Merlet, David T. Limmer, Mathieu Salanne, René van Roij, Paul A. Madden, David Chandler, and Benjamin Rotenberg. The electric double layer has a life of its own. *The Journal of Physical Chemistry C*, 118(32):18291–18298, 2014.

[3] Peng Li, Yuzhou Jiao, Jun Huang, and Shengli Chen. Electric double layer effects in electrocatalysis: Insights from ab initio simulation and hierarchical continuum modeling. *JACS Au*, 3(10):2640–2659, 2023.

[4] Lixin Su, Junxiang Chen, Fulin Yang, Peng Li, Yiming Jin, Wei Luo, and Shengli Chen. Electric-double-layer origin of the kinetic ph effect of hydrogen electrocatalysis revealed by a universal hydroxide adsorption-dependent inflection-point behavior. *Journal of the American Chemical Society*, 145(22):12051–12058, 2023. PMID: 37218973.

[5] Peng Li, Yaling Jiang, Youcheng Hu, Yana Men, Yuwen Liu, Wenbin Cai, and Shengli Chen. Hydrogen bond network connectivity in the electric double layer dominates the kinetic ph effect in hydrogen electrocatalysis on pt. *Nature Catalysis*, 5(10):900–911, 2022.

[6] Seung-Jae Shin, Dong Hyun Kim, Geunsu Bae, Stefan Ringe, Hansol Choi, Hyung-Kyu Lim, Chang Hyuck Choi, and Hyungjun Kim. On the importance of the electric double layer structure in aqueous electrocatalysis. *Nature Communications*, 13(1):174, 2022.

[7] Isis Ledezma-Yanez, W. David Z. Wallace, Paula Sebastián-Pascual, Victor Climent, Juan M. Koper, Feliu, and Marc T. M. Koper. Interfacial water reorganization as a ph-dependent descriptor of the hydrogen evolution rate on platinum electrodes. *Nature Energy*, 7(17031):17031, 2017.

[8] Thomas Mairegger, Haobo Li, Christoph Grießer, Daniel Winkler, Jakob Filser, Nicolas G. Hörmann, Karsten Reuter, and Julia Kunze-Liebhäuser. Electroreduction of co2 in a non-aqueous electrolyte-the generic role oacetonitrile. *ACS Catalysis*, 13(9):5780–5786, 2023.

[9] Yirui Zhang, Tao Wang, Livia Giordano, Dimitrios Fraggedakis, Botao Huang, Ryan Stephens, Martin Z. Bazant, and Yang Shao-Horn. (energy technology division

graduate student award sponsored by biologic) probing and engineering electrode-electrolyte interfaces in electrochemical energy storage and conversion. *ECS Meeting Abstracts*, MA2023-01(38):2249, aug 2023.

[10] Nicolas Dubouis, Alessandra Serva, Roxanne Berthin, Guillaume Jeanmairet, Benjamin Porcheron, Elodie Salager, Mathieu Salanne, and Alexis Grimaud. Tuning water reduction through controlled nanoconfinement within an organic liquid matrix. *Nature Catalysis*, 3(8):656–663, 2020.

[11] Christoph Gütz, Andreas Stenglein, and Siegfried R. Waldvogel. Highly modular flow cell for electroorganic synthesis. *Org. Process Res. Dev.*, 21(5):771–778, 2017.

[12] Giovanni Bussi, Davide Donadio, and Michele Parrinello. Canonical sampling through velocity rescaling. *J. Chem. Phys.*, 126(1):014101, 2007.

[13] Frank H. Stillinger and Thomas A. Weber. Packing structures and transitions in liquids and solids. *Science*, 225(4666):983–989, 1984.

[14] Daan Frenkel and Berend Smit. *Understanding Molecular Simulation: From Algorithms to Applications*. Academic Press, Inc., USA, 1st edition, 1996.

[15] Søren Toxvaerd. Hamiltonians for discrete dynamics. *Phys. Rev. E*, 50:2271–2274, Sep 1994.

[16] M. Parrinello and A. Rahman. Polymorphic transitions in single crystals: A new molecular dynamics method. *Journal of Applied Physics*, 52(12):7182–7190, 12 1981.

[17] Ryogo Kubo. Statistical-mechanical theory of irreversible processes. i. general theory and simple applications to magnetic and conduction problems. *Journal of the Physical Society of Japan*, 12(6):570–586, 1957.

[18] R Kubo. The fluctuation-dissipation theorem. *Reports on Progress in Physics*, 29(1):255, jan 1966.

[19] J E Lennard-Jones. Cohesion. *Proceedings of the Physical Society*, 43(5):461, sep 1931.

[20] Berk Hess, Carsten Kutzner, David van der Spoel, and Erik Lindahl. Gromacs 4:algorithms for highly efficient, load-balanced, and scalable molecular simulation. *Journal of Chemical Theory and Computation*, 4(3):435–447, 2008. PMID: 26620784.

[21] Robert J. Ouellette and J. David Rawn. 1 - structure and bonding in organic compounds. In Robert J. Ouellette and J. David Rawn, editors, *Organic Chemistry*, pages 1–39. Elsevier, Boston, 2014.

[22] Harold F. Hemond and Elizabeth J. Fechner. Chemical fate and transport in the environment (third edition). *Academic Press*, pages 1–476, 2015.

[23] D. Berthelot. "sur le mélange des gaz". *Comptes rendus hebdomadaires des séances de l'Académie des Sciences*, 26(16):1703–1855, 1898.

[24] David A. Case, Thomas E. Cheatham III, Tom Darden, Holger Gohlke, Ray Luo, Kenneth M. Merz Jr., Alexey Onufriev, Carlos Simmerling, Bing Wang, and Robert J. Woods. The amber biomolecular simulation programs. *Journal of Computational Chemistry*, 26(16):1668–1688, 2005.

[25] Yoshiteru Yonetani. Dielectric continuum model examination of real-space electrostatic treatments. *The Journal of Chemical Physics*, 154(4):044103, 01 2021.

[26] Berk Hess, Henk Bekker, Herman J. C. Berendsen, and Johannes G. E. M. Fraaije. Lincs: A linear constraint solver for molecular simulations. *J. Comput. Chem.*, 18(12):1463–1472.

[27] H. J. C. Berendsen, J. P. M. Postma, W. F. van Gunsteren, and J. Hermans. *Interaction Models for Water in Relation to Protein Hydration*, pages 331–342. Springer Netherlands, Dordrecht, 1981.

[28] H. J. C. Berendsen, J. R. Grigera, and T. P. Straatsma. The missing term in effective pair potentials. *The Journal of Physical Chemistry*, 91(24):6269–6271, 1987.

[29] J. L. F. Abascal and C. Vega. A general purpose model for the condensed phases of water: TIP4P/2005. *The Journal of Chemical Physics*, 123(23):234505, 12 2005.

[30] A.J.C. Ladd. Long-range dipolar interactions in computer simulations of polar liquids. *Molecular Physics*, 36(2):463–474, 1978.

[31] S. W. de Leeuw, J. W. Perram, E. R. Smith, and John Shipley Rowlinson. Simulation of electrostatic systems in periodic boundary conditions. i. lattice sums and dielectric constants. *Proc. Royal Soc. London*, 373(1752):27–56, 1980.

[32] J. M. Caillol, D. Levesque, and J. J. Weis. Electrical properties of polarizable ionic solutions. i. theoretical aspects. *J. Chem. Phys.*, 91(9):5544–5554, 1989.

[33] Markus Deserno and Christian Holm. How to mesh up ewald sums. i. a theoretical and numerical comparison of various particle mesh routines. *The Journal of Chemical Physics*, 109(18):7678–7693, 1998.

[34] Gerhard Hummer, Lawrence R. Pratt, Angel E. Garcıa, and Martin Neumann. Treatment of electrostatic interactions in computer simulations and calculation of thermodynamic properties such as free energies and pressures. *AIP Conference Proceedings*, 492(1):84–103, 11 1999.

[35] P. Wirnsberger, D. Fijan, A. Šarić, M. Neumann, C. Dellago, and D. Frenkel. Non-equilibrium simulations of thermally induced electric fields in water. *The Journal of Chemical Physics*, 144(22):224102, 06 2016.

[36] M. Neumann and O. Steinhauser. On the calculation of the dielectric constant using the ewald-kornfeld tensor. *Chemical Physics Letters*, 95(4):417–422, 1983.

[37] O. Steinhauser. Reaction field simulation of water. *Molecular Physics*, 45(2):335–348, 1982.

[38] Jr. Stillinger, Frank H. and Ronald Lovett. General Restriction on the Distribution of Ions in Electrolytes. *The Journal of Chemical Physics*, 49(5):1991–1994, 09 2003.

[39] S.W. De Leeuw and J.W. Perram. Computer simulation of ionic systems. influence of boundary conditions. *Physica A: Statistical Mechanics and its Applications*, 107(1):179–189, 1981.

[40] In-Chul Yeh and Max L. Berkowitz. Ewald summation for systems with slab geometry. *The Journal of Chemical Physics*, 111(7):3155–3162, 08 1999.

[41] James E. Roberts and Jurgen Schnitker. Boundary conditions in simulations of aqueous ionic solutions: A systematic study. *The Journal of Physical Chemistry*, 99(4):1322–1331, 1995.

[42] Ulrich Essmann, Lalith Perera, Max L. Berkowitz, Tom Darden, Hsing Lee, and Lee G. Pedersen. A smooth particle mesh Ewald method. *The Journal of Chemical Physics*, 103(19):8577–8593, 11 1995.

[43] R.W. Hockney and J.W. Eastwood. *Computer Simulation Using Particles*. 1988.

[44] Lars Onsager. Electric moments of molecules in liquids. *Journal of the American Chemical Society*, 58(8):1486–1493, 1936.

[45] V. Ballenegger and J.-P. Hansen. Dielectric permittivity profiles of confined polar fluids. *The Journal of Chemical Physics*, 122(11):114711, 03 2005.

[46] Berk Hess, Carsten Kutzner, David van der Spoel, and Erik Lindahl. Gromacs 4: Algorithms for highly efficient, load-balanced, and scalable molecular simulation. *J. Chem. Theory Comput.*, 4(3):435–447, 2008.

[47] A. P. Thompson, H. M. Aktulga, R. Berger, D. S. Bolintineanu, W. M. Brown, P. S. Crozier, P. J. in 't Veld, A. Kohlmeyer, S. G. Moore, T. D. Nguyen, R. Shan, M. J. Stevens, J. Tranchida, C. Trott, and S. J. Plimpton. LAMMPS - a flexible simulation tool for particle-based materials modeling at the atomic, meso, and continuum scales. *Comp. Phys. Comm.*, 271:108171, 2022.

[48] Yizhak Marcus. The structure of and interactions in binary acetonitrile plus water mixtures. *J. Phys. Org. Chem.*, 25(12):1072–1085, DEC 2012.

[49] Colette Moreau and Gérard Douhéret. Thermodynamic behavior of water-acetonitrile mixtures excess volumes and viscosities. *Thermochimica Acta*, 13(4):385–392, 1975.

[50] M. Stähelin, C. R. Moylan, D. M. Burland, A. Willetts, J. E. Rice, D. P. Shelton, and E. A. Donley. A comparison of calculated and experimental hyperpolarizabilities for acetonitrile in gas and liquid phases. *J. Chem. Phys.*, 98(7):5595–5603, April 1993.

[51] John E. Bertie and Zhida Lan. Liquid Water-Acetonitrile Mixtures at 25 °C: The Hydrogen-Bonded Structure Studied through Infrared Absolute Integrated Absorption Intensities. *J. Phys. Chem. B*, 101(20):4111–4119, May 1997.

[52] DS Venables and CA Schmuttenmaer. Spectroscopy and dynamics of mixtures of water with acetone, acetonitrile, and methanol. *J. Chem. Phys.*, 113(24):11222–11236, DEC 22 2000.

[53] I Bako, T Megyes, and G Palinkas. Structural investigation of water-acetonitrile mixtures: An ab initio, molecular dynamics and x-ray diffraction study. *Chem. Phys.*, 316(1-3):235–244, SEP 19 2005.

[54] I Bako, T Megyes, T Grosz, G Palinkas, and J Dore. Structural investigation of water-acetonitrile mixtures: Small-angle and wide-angle neutron diffraction study compared to molecular dynamics simulation. *J. Mol. Liquids*, 125(2-3):174–180, APR 15 2006. EMLG/JMLG Conference on Complex Liquids - Fundamental Properties to Industrial Applications, Sheffield, ENGLAND, SEP 03-07, 2004.

[55] Feng Ding, Zhonghan Hu, Qin Zhong, Katherine Manfred, Rafael R. Gattass, Michael R. Brindza, John T. Fourkas, Robert A. Walker, and John D. Weeks. Interfacial Organization of Acetonitrile: Simulation and Experiment. *J. Phys. Chem. C*, 114(41):17651–17659, October 2010.

[56] Masanari Nagasaka, Hayato Yuzawa, and Nobuhiro Kosugi. Microheterogeneity in Aqueous Acetonitrile Solution Probed by Soft X-ray Absorption Spectroscopy. *J. Phys. Chem. B*, 124(7):1259–1265, February 2020.

[57] Samuel R. Cohen, Marie Plazanet, Stéphane Rols, David J. Voneshen, John T. Fourkas, and Benoit Coasne. Structure and dynamics of acetonitrile: Molecular simulation and neutron scattering. *J. Mol. Liquids*, 348:118423, February 2022.

[58] M. Matsumoto, H. Tanaka, and K. Nakanishi. Acteonitrile pair formation in aqueous solution. *J. Chem. Phys.*, 99(9):6935–6940, NOV 1 1993.

[59] Y. Satoh and K. Nakanishi. Theoretical studies of acetonitrile-water mixtures / monte carlo simulation. *Fluid Phase Equilibria*, 104:41–55, MAR 1 1995. 1st International Conference on Molecular Thermodynamics and Molecular Simulation, KYOTO UNIV, KYOTO, JAPAN, JAN 09-13, 1994.

[60] H. Reis, M. G. Papadopoulos, and A. Avramopoulos. Calculation of the Microscopic and Macroscopic Linear and Nonlinear Optical Properties of Liquid Acetonitrile. I. Accurate Molecular Properties in the Gas Phase and Susceptibilities of the Liquid in Onsager' s Reaction-Field Model. *J. Phys. Chem. C*, 107(19):3907–3917, 2003.

[61] H. Kovacs and A. Laaksonen. Molecular-dynamics simulation and NMR-study of water acetonitrile mixtures. *J. Am. Chem. Soc.*, 113(15):5596–5605, JUL 17 1991.

[62] DL Bergman and A Laaksonen. Topological and spatial structure in the liquid-water-acetonitrile mixture. *Phys. Rev. E*, 58(4):4706–4715, OCT 1998.

[63] RD Mountain. Molecular dynamics study of water-acetonitrile mixtures. *J. Phys. Chem. A*, 103(50):10744–10748, DEC 16 1999.

[64] C Oldiges, K Wittler, T Tonsing, and A Alijah. Md calculated structural properties of clusters in liquid acetonitrile/water mixtures with various contents of acetonitrile. *J. Phys. Chem. A*, 106(31):7147–7154, AUG 8 2002.

[65] A. Avramopoulos, M. G. Papadopoulos, and H. Reis. Calculation of the Microscopic and Macroscopic Linear and Nonlinear Optical Properties of Liquid Acetonitrile. II. Local Fields and Linear and Nonlinear Susceptibilities in Quadrupolar Approximation. *J. Phys. Chem. B*, 111(10):2546–2553, March 2007.

[66] Alexander Y. Zasetsky, Svetlana V. Petelina, Andrey K. Lyashchenko, and Alexander S. Lileev. Computer simulation study of rotational diffusion in polar liquids of different types. *J. Chem. Phys.*, 133(13):134502, October 2010.

[67] Raymond D. Mountain. Microstructure and hydrogen bonding in water-acetonitrile mixtures. *J. Phys. Chem. B*, 114(49):16460–16464, DEC 16 2010.

[68] Jinfan Chen and Patrick H. L. Sit. Ab initio study of the structural properties of acetonitrile-water mixtures. *Chem. Phys.*, 457:87–97, AUG 18 2015.

[69] Michael J. Makowski, Abraham C. Stern, John C. Hemminger, and Douglas J. Tobias. Orientation and Structure of Acetonitrile in Water at the Liquid–Vapor Interface: A Molecular Dynamics Simulation Study. *J. Phys. Chem. C*, 120(31):17555–17563, August 2016.

[70] Szilvia Pothoczki and Laszlo Pusztai. Intermolecular orientations in liquid acetonitrile: New insights based on diffraction measurements and all-atom simulations. *J. Mol. Liquids*, 225:160–166, JAN 2017.

[71] Isaak N. Daniels, Zhenxing Wang, and Brian B. Laird. Dielectric Properties of Organic Solvents in an Electric Field. *J. Phys. Chem. C*, 121(2):1025–1031, January 2017.

[72] Sonia M. Aguilera-Segura, Francesco Di Renzo, and Tzonka Mineva. Structures, intermolecular interactions, and chemical hardness of binary water–organic solvents: a molecular dynamics study. *J. Mol. Modeling*, 24(10):292, September 2018.

[73] Zuzana Sochorova Vokacova and Eva Pluharova. Understanding structure and dynamics of organic liquid mixtures by molecular simulations. *J. Mol. Liquids*, 288, AUG 15 2019.

[74] Oliver R. Gittus, Pablo Albella, and Fernando Bresme. Polarization of acetonitrile under thermal fields via non-equilibrium molecular dynamics simulations. *J. Chem. Phys.*, 153(20):204503, NOV 28 2020.

[75] H. J. Böhm, I. R. McDonald, and P. A. Madden. An effective pair potential for liquid acetonitrile. *Mol. Phys.*, 49(2):347–360, 1983.

[76] W. L. Jorgensen and J. M. Briggs. Monte-carlo simulations of liquid acetonitrile with a 3-site model. *Molecular Physics*, 63(4):547–558, MAR 1988.

[77] X Grabuleda, C Jaime, and PA Kollman. Molecular dynamics simulation studies of liquid acetonitrile: New six-site model. *J. Comput. Chem.*, 21(10):901–908, JUL 30 2000.

[78] Alexei M. Nikitin and Alexander P. Lyubartsev. New six-site acetonitrile model for simulations of liquid acetonitrile and its aqueous mixtures. *J. Comput. Chem.*, 28(12):2020–2026, SEP 2007.

[79] Volodymyr A. Koverga, Oleksandr M. Korsun, Oleg N. Kalugin, Bogdan A. Marekha, and Abdenacer Idrissi. A new potential model for acetonitrile: Insight into the local structure organization. *J. Mol. Liquids*, 233:251–261, MAY 2017.

[80] Mohammad H. Kowsari and Leila Tohidifar. Systematic evaluation and refinement of existing all-atom force fields for the simulation of liquid acetonitrile. *J. Comput. Chem.*, 39(23):1843–1853, SEP 5 2018.

[81] Roxanne Berthin, Alessandra Serva, Kyle G. Reeves, Esther Heid, Christian Schröder, and Mathieu Salanne. Solvation of anthraquinone and TEMPO redox-active species in acetonitrile using a polarizable force field. *J. Chem. Phys.*, 155(7):074504, August 2021.

[82] Jesse G. McDaniel. Polarization Effects in Binary [BMIM+][BF4–]/1,2-Dichloroethane, Acetone, Acetonitrile, and Water Electrolytes. *J. Phys. Chem. B*, 122(15):4345–4355, April 2018. Publisher: American Chemical Society.

[83] Imre Bakó, Tünde Megyes, Szabolcs Bálint, Tamás Grósz, and Viorel Chihaia. Water–methanol mixtures: topology of hydrogen bonded network. *Phys. Chem. Chem. Phys.*, 10:5004–5011, 2008.

[84] Giuseppe Cassone, Paolo V. Giaquinta, Franz Saija, and A. Marco Saitta. Liquid methanol under a static electric field. *J. Chem. Phys.*, 142(5):054502, February 2015.

[85] Giuseppe Cassone. Nuclear Quantum Effects Largely Influence Molecular Dissociation and Proton Transfer in Liquid Water under an Electric Field. *J. Phys. Chem. Lett.*, 11(21):8983–8988, November 2020. Publisher: American Chemical Society.

[86] Giuseppe Cassone, Adriano Sofia, Jiri Sponer, A. Marco Saitta, and Franz Saija. Ab Initio Molecular Dynamics Study of Methanol-Water Mixtures under External Electric Fields. *Molecules*, 25(15):3371, January 2020. Number: 15 Publisher: Multidisciplinary Digital Publishing Institute.

[87] Giuseppe Cassone, Jiri Sponer, and Franz Saija. Ab Initio Molecular Dynamics Studies of the Electric-Field-Induced Catalytic Effects on Liquids. *Top. Catal.*, 65(1):40–58, February 2022.

[88] Valeria Conti Nibali, Sthitadhi Maiti, Franz Saija, Matthias Heyden, and Giuseppe Cassone. Electric-field induced entropic effects in liquid water. *J. Chem. Phys.*, 158(18):184501, May 2023.

[89] Christopher A. Petroff, Giuseppe Cassone, Jiří Šponer, and Geoffrey R. Hutchison. Intrinsically Polar Piezoelectric Self-Assembled Oligopeptide Monolayers. *Advanced Materials*, 33(17):2007486, 2021. _eprint: https://onlinelibrary.wiley.com/doi/pdf/10.1002/adma.202007486.

[90] Sason Shaik, Debasish Mandal, and Rajeev Ramanan. Oriented electric fields as future smart reagents in chemistry. *Nat. Chem.*, 8(12):1091–1098, December 2016. Number: 12 Publisher: Nature Publishing Group.

[91] Sason Shaik, David Danovich, Jyothish Joy, Zhanfeng Wang, and Thijs Stuyver. Electric-Field Mediated Chemistry: Uncovering and Exploiting the Potential of (Oriented) Electric Fields to Exert Chemical Catalysis and Reaction Control. *J. Am. Chem. Soc.*, 142(29):12551–12562, July 2020. Publisher: American Chemical Society.

[92] Giuseppe Cassone, Adriano Sofia, Giovanni Rinaldi, and Jiri Sponer. Catalyst-Free Hydrogen Synthesis from Liquid Ethanol: An ab Initio Molecular Dynamics Study. *J. Phys. Chem. C*, 123(14):9202–9208, April 2019. Publisher: American Chemical Society.

[93] William L. Jorgensen, Jayaraman Chandrasekhar, Jeffry D. Madura, Roger W. Impey, and Michael L. Klein. Comparison of simple potential functions for simulating liquid water. *J. Chem. Phys.*, 79(2):926–935, 1983.

[94] Massimiliano Stengel, Nicola A. Spaldin, and D. Vanderbilt. Electric displacement as the fundamental variable in electronic-structure calculations. *Nature Physics*, 5:304–308, 2009.

[95] Chao Zhang and Michiel Sprik. Computing the dielectric constant of liquid water at constant dielectric displacement. *Phys. Rev. B*, 93:144201, 2016.

[96] Chao Zhang, Jürg Hutter, and Michiel Sprik. Computing the kirkwood g-factor by combining constant maxwell electric field and electric displacement simulations: Application to the dielectric constant of liquid water. *J. Phys. Chem. Lett.*, 7(14):2696–2701, JUL 21 2016.

[97] Tom Darden, Darrin York, and Lee Pedersen. Particle mesh ewald: An nlog(n) method for ewald sums in large systems. *J. Chem. Phys.*, 98(12):10089–10092, 1993.

[98] Mats Ormö, Andrew B. Cubitt, Karen Kallio, Larry A. Gross, Roger Y. Tsien, and S. James Remington. Crystal structure of the aequorea victoria green fluorescent protein. *Science*, 273(5280):1392–1395, 1996.

[99] L. Martínez, R. Andrade, E. G. Birgin, and J. M. Martínez. Packmol: A package for building initial configurations for molecular dynamics simulations. *J. Comput. Chem.*, 30(13):2157–2164, 2009.

[100] M. Brehm, M. Thomas, S. Gehrke, and B. Kirchner. Travis—a free analyzer for trajectories from molecular simulation. *J. Chem. Phys.*, 152(16):164105, 2020.

[101] Wendy D. Cornell, Piotr Cieplak, Christopher I. Bayly, Ian R. Gould, Kenneth M. Merz, David M. Ferguson, David C. Spellmeyer, Thomas Fox, James W. Caldwell, and Peter A. Kollman. A Second Generation Force Field for the Simulation of Proteins, Nucleic Acids, and Organic Molecules. *ACS Publications*, May 2002.

[102] John David Jackson. *Classical Electrodynamics*. Wiley; 3rd edition, 1998.

[103] Jean-Michel Caillol. Comments on the numerical simulations of electrolytes in periodic boundary conditions. *J. Chem. Phys.*, 101(7):6080–6090, 1994.

[104] Leonardo G. Gagliardi, Cecilia B. Castells, Clara Rafols, Marti Roses, and Elisabeth Bosch. Static Dielectric Constants of Acetonitrile/Water Mixtures at Different Temperatures and Debye Hückel A and a_0B Parameters for Activity Coefficients. *J. Chem. Eng. Data*, 52:1103–1107, 2007. Publisher: American Chemical Society.

[105] Karl Schönbach, Jürgen Kolb, Shu Xiao, Sunao Katsuki, Yasushi Minamitani, and Ravindra Joshi. Electrical breakdown of water in microgaps. *Plasma Sources Science and Technology*, 17(2):024010, 2008.

[106] Masakazu Matsumoto. Relevance of hydrogen bond definitions in liquid water. *J. Chem. Phys.*, 126(5):054503, February 2007.

[107] Imre Bakó, Dániel Csókás, and Szilvia Pothoczki. Molecular aggregation in liquid water: Laplace spectra and spectral clustering of h-bonded network. *J. Mol. Liquids*, 327:114802, 2021.

[108] Eric F Pettersen, Thomas D Goddard, Conrad C Huang, Gregory S Couch, Daniel M Greenblatt, Elaine C Meng, and Thomas E Ferrin. Ucsf chimera–a visualization system for exploratory research and analysis. *J. Comput. Chem.*, 25(13):1605—1612, October 2004.

[109] James E. J. Mills and Philip M. Dean. Three-dimensional hydrogen-bond geometry and probability information from a crystal survey. *J. Comput. Aided Mol. Des.*, 10:607–622, 1996.

[110] R. Gopi, N. Ramanathan, and K. Sundararajan. Acetonitrile-water hydrogen-bonded interaction: Matrix-isolation infrared and ab initio computation. *J. Mol. Struct.*, 1094:118–129, 2015.

Appendix A

Supplementary information

A.1 Force field parameters of the Kowsari force field

Below, we reproduce the force field parameters of the Kowsari force field [80], which is used in most of the simulations. The labelling convention for C-atoms is shown in Figure A.1.

Table A.1 Force field parameters for the CCN molecule[80]

[atoms] *name*	*atomic number*	*mass* $[a.m.u.]$	*charge* $[e]$	σ $[nm]$	ε $[kj/mol]$
N1	7	14.01	-0.5126	3.33700e-01	6.99860e-01
C1	6	12.01	0.4917	3.75290e-01	4.84670e-01
C2	6	12.01	-0.5503	3.39960e-01	4.57720e-01
H21	1	1.008	0.1904	2.45510e-01	1.00000e-05
H22	1	1.008	0.1904	2.45510e-01	1.00000e-05
H23	1	1.008	0.1904	2.45510e-01	1.00000e-05

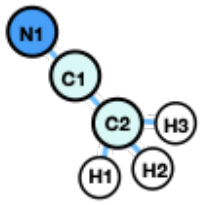

Figure A.1 Two dimensional representation of the acetonitrile molecule.

A.2 Hydrogen bond analysis

As mentioned in the main text, we use the CHIMERA [108] software to analyze the hydrogen bond network in our configurations. Figure A.2 shows a schematic description how this is done. The first step is to identify close intermolecular contacts by searching in a spherical region centered in a donor site (X) potential acceptor sites (Y), such that their distance (r) is less than 4.5 Å with a tolerance of 3.5 Å, and the X-H$\cdots$Y (θ) angle is larger than 90° with a tolerance of 30°. The geometric parameters (e.g., distances and angles) are then split into intervals of equal volume that define bins, allowing the calculation of frequency distributions of the geometric parameters. A density of points represents the hydrogen bonds and, therefore, the probability of observing a hydrogen bond in that bin. The frequency distribution analysis continues until background noise appears, and then two statistical tests are used to determine the cutoff values for r, ϕ, θ (in spherical coordinates).

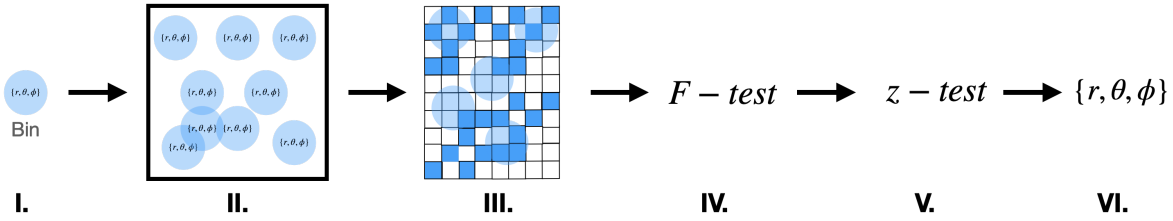

Figure A.2 Schematic description of the calculations of hydrogen bonds using the CHIMERA tool. **I**. First, identification of close intermolecular contacts using r <4.5 Å and $\theta > 90°$ takes place. **II**. Bins are defined by splitting the geometrical parameters into intervals of equal volume and are within the simulation box. **III**. Density of points represents hydrogen bonds and, therefore, the probability of observing a hydrogen bond in that bin. Blue squares represent hydrogen bonds, and blared blue background circles are a 2D representation of the bins. **IV**. and **V** A frequency distribution analysis followed by two further statistical tests to determine cutoff values for r, ϕ and θ (in spherical coordinates) **VI**.. Iteration of these steps, (**I**. $\leftrightarrow$ **VI**.) provides the final cutoff parameters.[109]

A.3 Additional data for radial distribution functions

A.3.1 Atom-atom correlation functions at zero electric field and different CCN force fields

In order to compare different force fields to each other, we have computed atom-atom radial distribution functions (RDFs) for all atom types in our system. Some results are shown in the main text (Figures 3-5). Here, we show additional curves which were obtained from

simulations with four different force fields. The numbering convention for C-atoms in CCN (C_1, C_2) is the same as in Figure A.1. Figures A.3–A.6 show results obtained with SPC water. The last figure, Figure A.8, shows the RDF for the nitrogen atom of CCN and the hydrogen atom of water obtained with simulations using TIP4P water. This figure essentially reproduces the features which have already been observed with SPC water (Figure 4 in the main text): The main structure of the reference RDF curves from the ab-initio work of Chen and Sit[68] and the location of the peaks is correct, but the height of the first peak at large CCN concentration is vastly over estimated for all force fields except the Kowsari force field[80]. The figure also demonstrates that the data obtained with TIP4P water much more noisy than those obtained with SPC water, if the length of the analyzed trajectory (10 ns) is the same.

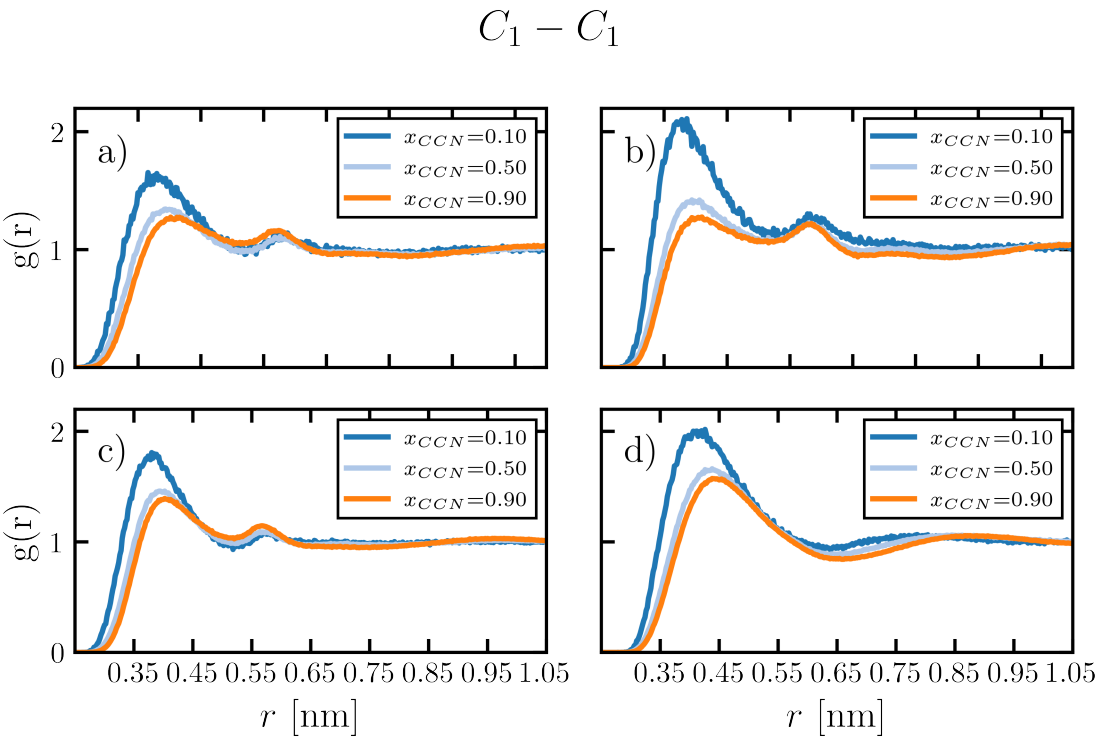

Figure A.3 $g(r)$ between the carbon atoms of the methyl group CH_3 of CCN from classical simulations obtained with the SPC water model and different CCN force fields: (a) Nikitin [78], (b) Grabuleda [77], (c) Koverga [79], (d) Kowsari [80].

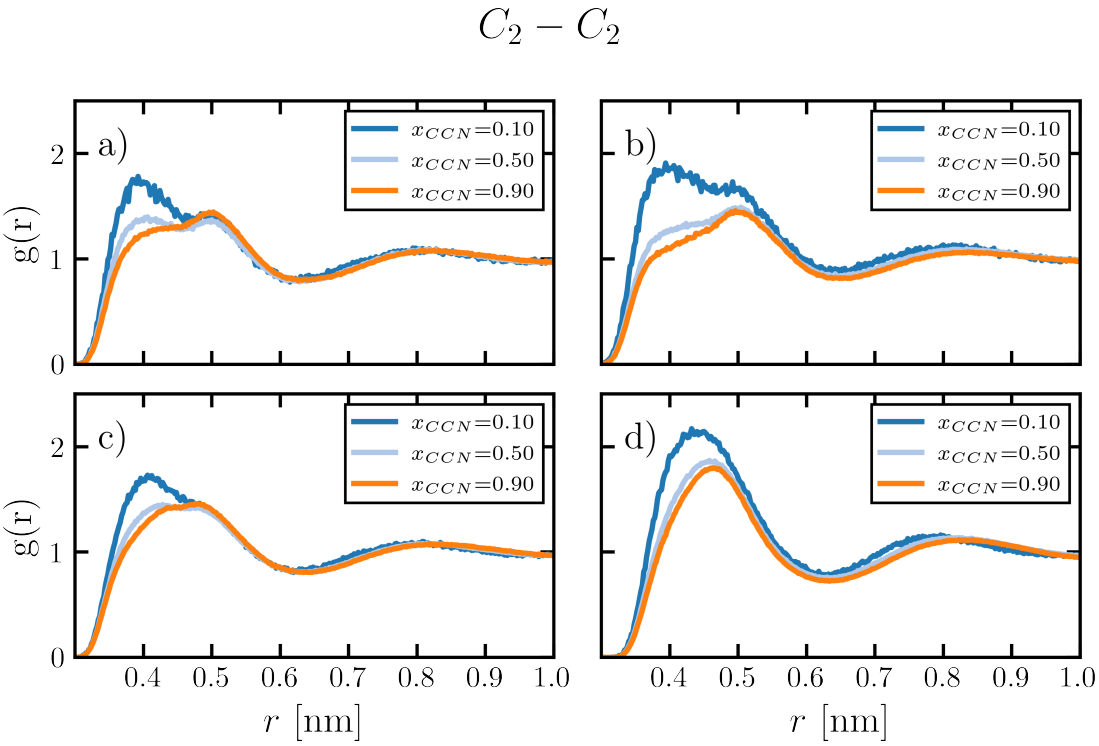

Figure A.4 Same as A.3 for the RDF between the carbon atoms of the *CN* group of CCN

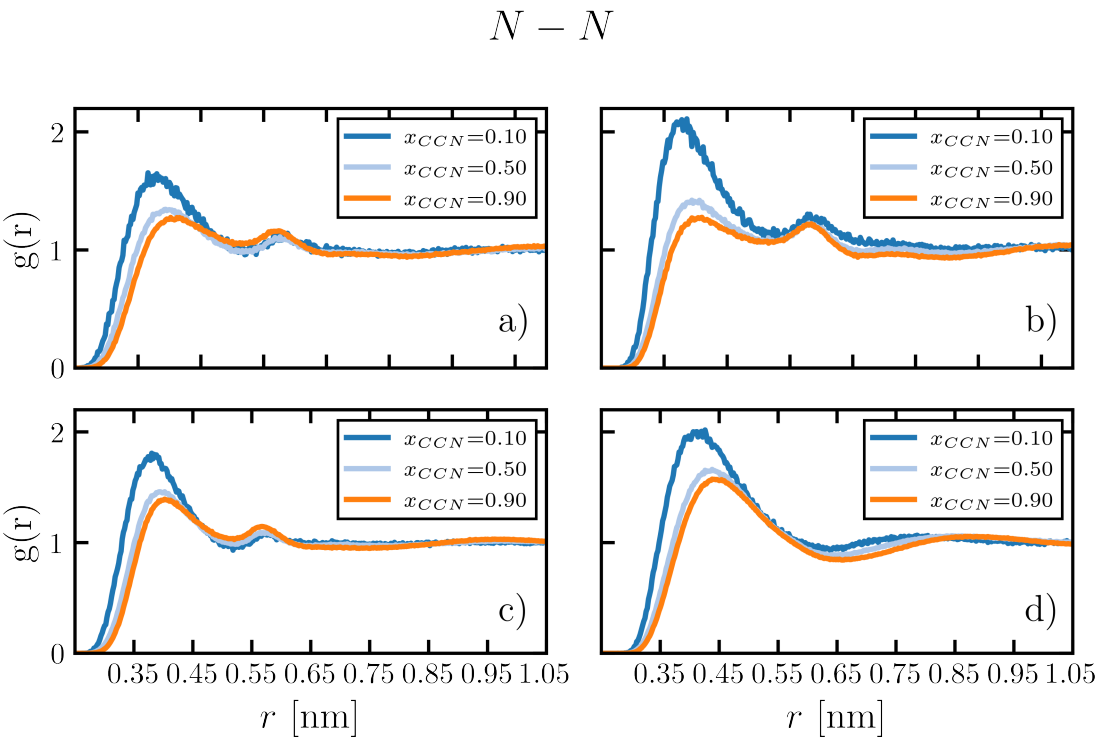

Figure A.5 Same as A.3 for the RDF between the nitrogen atoms of CCN.

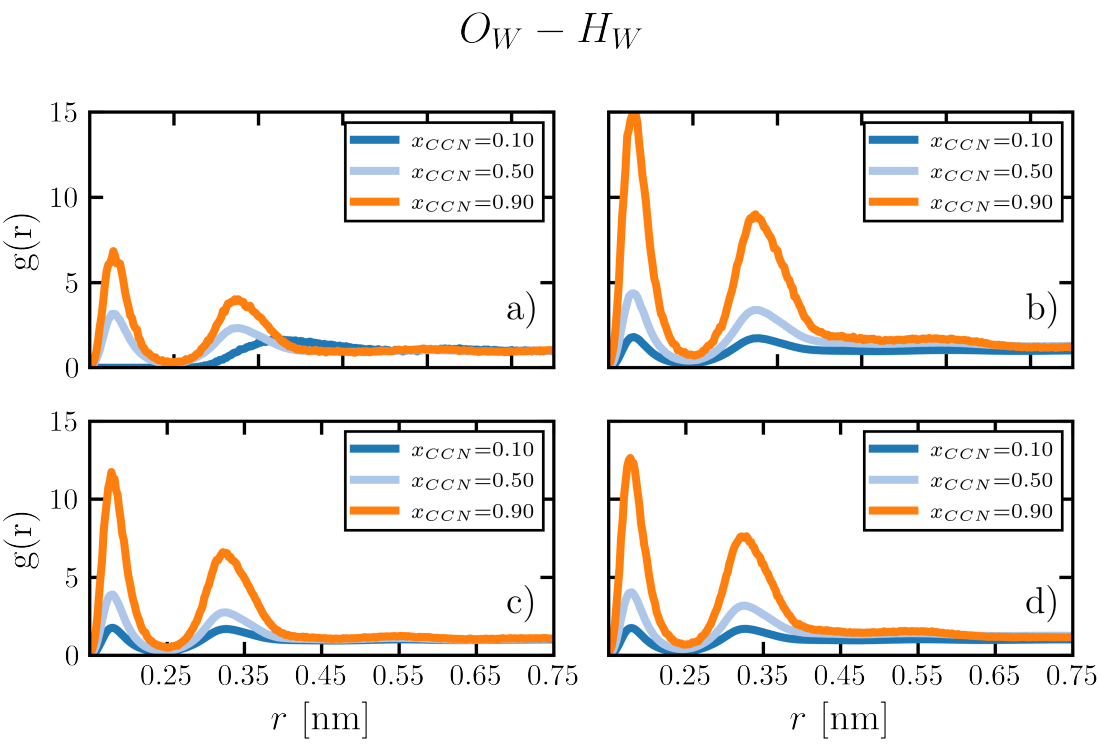

Figure A.6 Same as A.3 for the RDF between the oxygen and hydrogen atoms of water.

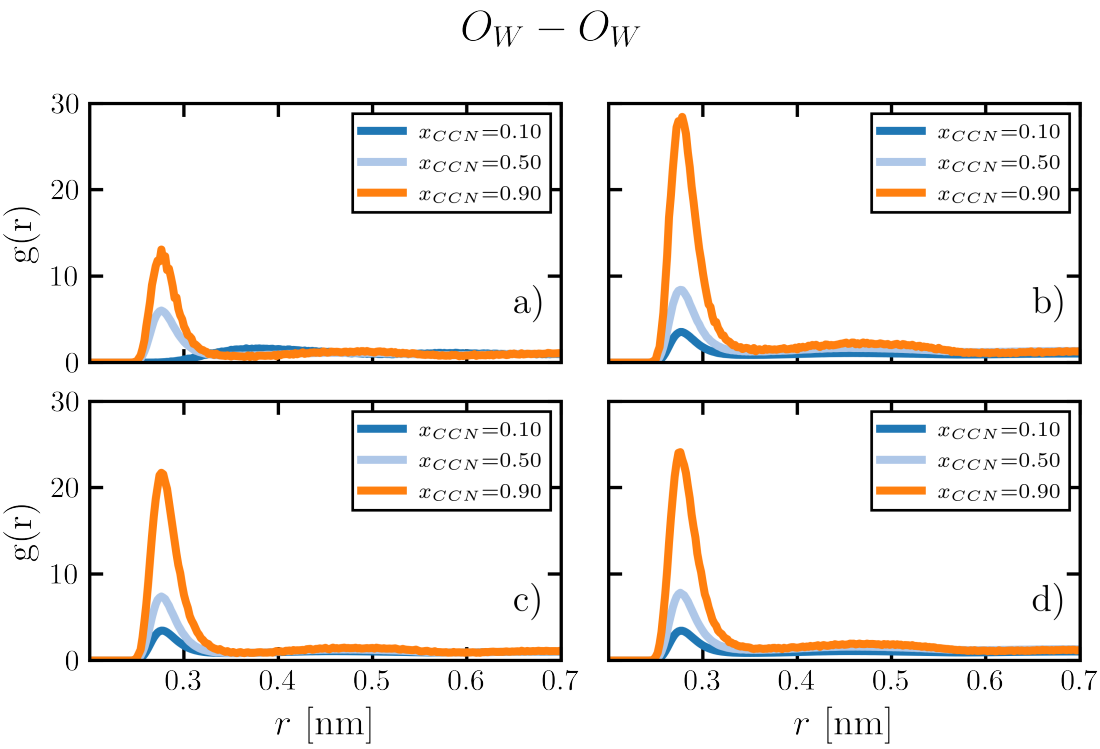

Figure A.7 Same as A.3 for the RDF between the oxygen atoms of water.

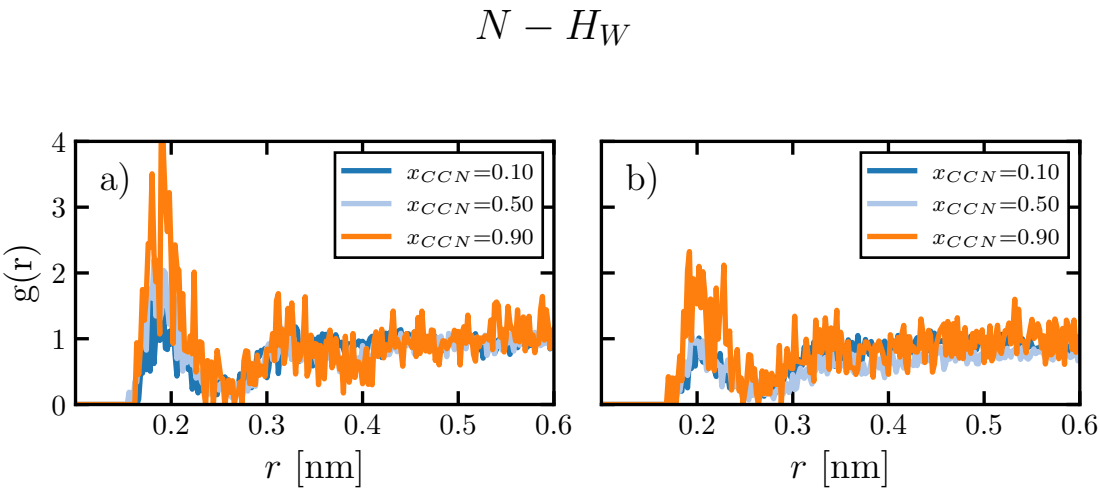

Figure A.8 RDF ($g(r)$) between the nitrogen atom of the CCN molecule and the hydrogen atoms of water obtained from classical simulations obtained with the TIP4P water model and different CCN force fields: (a) Koverga [79], (d) Kowsari [80].

A.3.2 Atom-atom correlation functions at nonzero electric field

Supplementing Figure 7 in the main text, we here show some additional data for atom-atom pair distribution functions at $x_{CCN} = 0.75$ under the influence of different electric fields. These simulations were done using the Kowsari force field [80] with SPC water. The labelling convention for C-atoms is again that of Figure A.1.

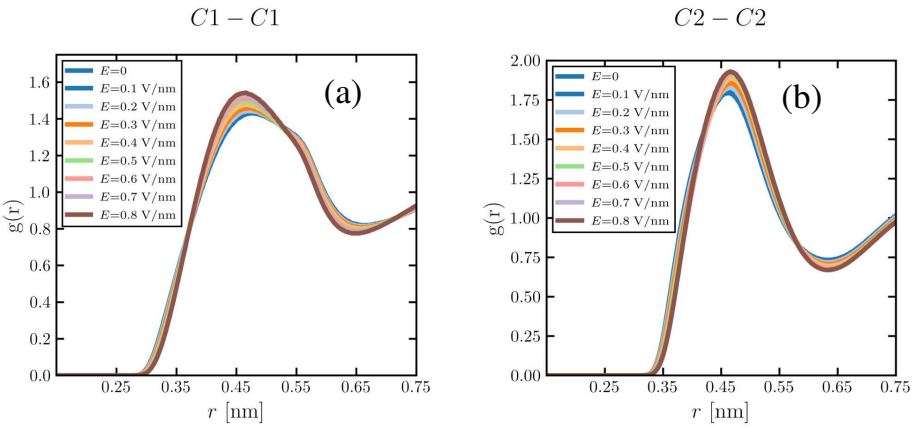

Figure A.9 Radial distribution functions between the carbon atoms of different CCN molecules

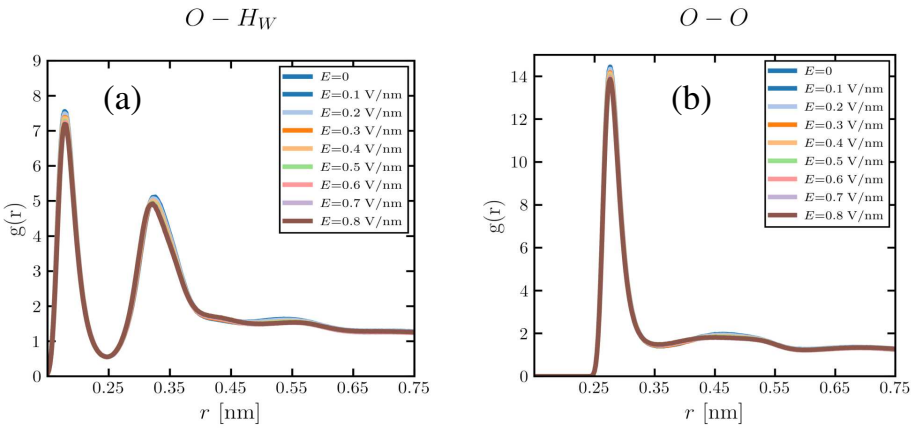

Figure A.10 Radial distribution functions between different atom pairs of hydrogen molecules

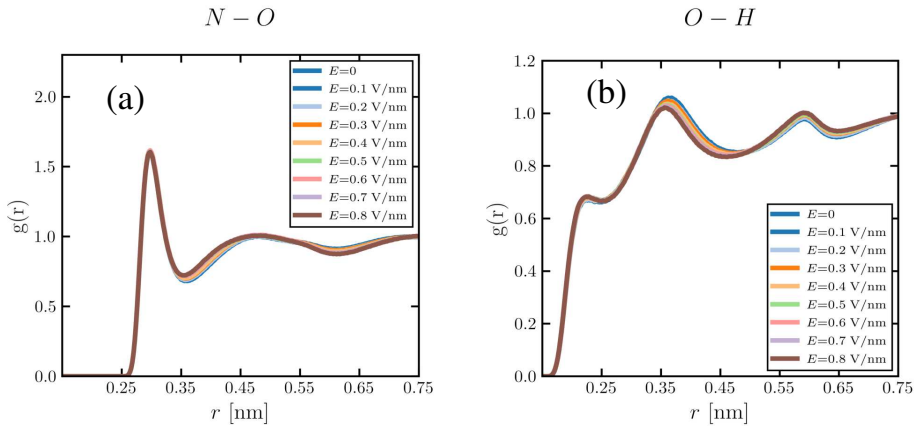

Figure A.11 Radial distribution function between (a) nitrogen and oxygen atoms in CCN molecules, and (b) CCN hydrogen and water oxigen.

A.3.3 Center-of-mass correlation functions at zero electric field

Finally, Figure A.12 shows the radial distribution function of the center-of-mass coordinates of CCN molecules at zero electric field. These data were again obtained with the Kowsari force field [80] and SPC water, at a CCN mole fraction of $x_{CCN} = 0.75$.

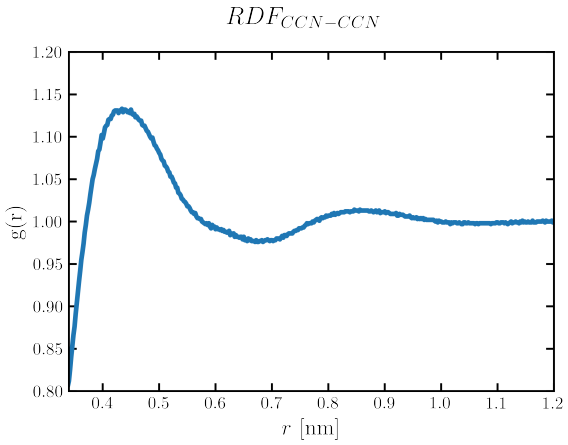

Figure A.12 Radial distribution function of the center-of-mass coordinates acetonitrile molecules in an aqueous mixture with a 75% mole fraction of CCN.

A.4 Effective dielectric constant

We consider a situation where a static macroscopic field **E** is imposed on a dielectric fluid in the nonlinear regime (the susceptibility $\chi(E) = \frac{1}{\varepsilon_0} P_0/E$ and the differential susceptibility

$\chi^d(E) = \frac{1}{\varepsilon_0} \mathrm{d}P_0/\mathrm{d}E$ are not constant), and study its impact on the effective interactions between free charges Q_i in the fluid. The interactions are associated with the work required for moving the charges away from each other, which is reduced due to the reorientation of dipoles in the fluid. In the nonlinear regime, the amplitude of the reorientations depends on the relative angle between the dipoles and the macroscopic field. As a consequence, the effective Coulomb interactions become anisotropic. This can be described by an anisotropic dielectric constant, i.e., a dielectric tensor $\underline{\underline{\varepsilon}}_{r,\mathrm{eff}}$. We derive an expression for $\underline{\underline{\varepsilon}}_{r,\mathrm{eff}}$ using a phenomenological approach.

Let $\rho_{\mathrm{free}}(\mathbf{r})$ denote the density of free charges. The Maxwell field $\mathbf{E}_M(\mathbf{r})$ at position $\mathbf{r}$ is given by $\mathbf{E}_M = \mathbf{E} + \mathbf{E}_{\mathrm{interactions}}$, where $\mathbf{E}$ denotes the macroscopic field and $\mathbf{E}_{\mathrm{interactions}}$ the electrostatic field of all charges in the fluid. The latter can be derived from a potential, $\mathbf{E}_{\mathrm{interactions}} = -\nabla\Phi$. (Note that the macroscopic field, $\mathbf{E}$, cannot be derived from a potential in a system with periodic boundaries, therefore it is not included in the above equation.)

The total dielectric displacement is hence given by $\mathbf{D}(\mathbf{r}) = \varepsilon_0 \mathbf{E}_M(\mathbf{r}) + \mathbf{P}$ with the polarization $\mathbf{P}$. This results in the Poisson equation

$$4\pi\rho_{\mathrm{free}} = \nabla\cdot\mathbf{D} = \nabla(\varepsilon_0\mathbf{E}_M(\mathbf{r}) + \mathbf{P}(\mathbf{r})) = -\nabla(\varepsilon_0\nabla\Phi - \mathbf{P}(\mathbf{r})), \tag{A.1}$$

where we have exploited $\nabla\cdot\mathbf{E} = 0$ since $\mathbf{E}$ is constant.

Next we insert $\mathbf{P} = \varepsilon_0\chi(E_M)\mathbf{E}_M$ with $\mathbf{E}_M = \mathbf{E} - \nabla\Phi$ and assume $|\nabla\Phi| \ll |\mathbf{E}|$ in the nonlinear regime. Expanding in powers of $|\nabla\Phi|$, we obtain

$$\begin{aligned}\frac{\mathbf{P}}{\varepsilon_0} &\approx \chi(E)\,\mathbf{E} - \chi'(E)\left(\frac{\mathbf{E}}{E}\cdot\nabla\Phi\right)\mathbf{E} - \chi(E)\,\nabla\Phi + \mathscr{O}(|\nabla\Phi|^2).\\ &= \frac{\mathbf{P}_0}{\varepsilon_0} - \underline{\underline{\chi}}_{\mathrm{eff}}\,\nabla\Phi\end{aligned}$$

with $\mathbf{P}_0 = \varepsilon_0\chi(E)\,\mathbf{E}$ and $\underline{\underline{\chi}}_{\mathrm{eff}} = \mathbf{1}\,\chi(E) + \hat{E}\hat{E}\,(\chi'(E)\,E)$, where $\hat{E} = \mathbf{E}/E$ and $\hat{E}\hat{E}$ denotes a tensor product. Using $\chi^d(E) = \frac{1}{\varepsilon_0}\mathrm{d}P_0/\mathrm{d}E = \chi(E) + \chi'(E)\,E$, this can be rewritten as

$$\underline{\underline{\chi}}_{\mathrm{eff}} = (\mathbf{1} - \hat{E}\hat{E})\,\chi(E) + \hat{E}\hat{E}\,\chi^d(E) \tag{A.2}$$

Thus the Poisson equation (A.1) for the interaction potential Φ, which defines the interactions between the free charges, can be rewritten as

$$\nabla\varepsilon_0\,\underline{\underline{\varepsilon}}_{r,\mathrm{eff}}(E)\,\nabla\Phi = \rho_{\mathrm{free}} \tag{A.3}$$

with the effective dielectric tensor

$$\underline{\underline{\varepsilon}}_{r,\mathrm{eff}}(E) = \mathbf{1} + \underline{\underline{\chi}}_{\mathrm{eff}}(E) = \mathbf{1} + (\mathbf{1} - \hat{E}\hat{E})\,\gamma(E) + \hat{E}\hat{E}\,\chi^{d}(E) \tag{A.4}$$